

FocDepthFormer: Transformer with LSTM for Depth Estimation from Focus

Xueyang Kang

PSI Department, ESAT faculty, KU Leuven
Kasteelpark Arenberg 10, Leuven 3001, Belgium

alex.kang@kuleuven.be

Abdur Fayjie

PSI Department, ESAT faculty, KU Leuven
Kasteelpark Arenberg 10, Leuven 3001, Belgium

abdurrazzaq.fayjie@kuleuven.be

Fengze Han

EI faculty, Technical University of Munich
Arcisstraße 21, Munich 80333, Germany

torresmilito22@gmail.com

Dong Gong

CS Engineering, The UNSW Sydney
Kensington NSW 2052, Australia

edgong01@gmail.com

Abstract

Depth estimation from focal stacks is a fundamental computer vision problem that aims to infer depth from focus/defocus cues in the image stacks. Most existing methods tackle this problem by applying convolutional neural networks (CNNs) with 2D or 3D convolutions over a set of fixed stack images to learn features across images and stacks. Their performance is restricted due to the local properties of the CNNs, and they are constrained to process a fixed number of stacks consistent in train and inference, limiting the generalization to the arbitrary length of stacks. To handle the above limitations, we develop a novel Transformer-based network, FocDepthFormer, composed mainly of a Transformer with an LSTM module and a CNN decoder. The self-attention in Transformer enables learning more informative features via an implicit non-local cross reference. The LSTM module is learned to integrate the representations across the stack with arbitrary images. To directly capture the low-level features of various degrees of focus/defocus, we propose to use multi-scale convolutional kernels in an early-stage encoder. Benefiting from the design with LSTM, our FocDepthFormer can be pre-trained with abundant monocular RGB depth estimation data for visual pattern capturing, alleviating the demand for the hard-to-collect focal stack data. Extensive experiments on various focal stack benchmark datasets show that our model outperforms the state-of-the-art models on multiple metrics.

1. Introduction

Depth estimation is a fundamental and challenging task for various computer vision applications, such as 3D scene understanding, image editing, and augmented/virtual reality. For convenience and flexibility, estimating pixel-wise depth from RGB images indirectly has been one of the core paradigms for perception, unlike direct depth measurements from Lidar scan [21]. To solve this problem, various cues have been explored to infer the depth information from the raw visual signal, such as image context [65, 66], geometric

cues [1, 4, 54, 63, 64], disparity from motion [56, 62], and focus/defocus cues [10, 11, 57]. With the advancement of deep neural networks (DNNs) and high-volume data being available, predicting depth from monocular images [65, 66] relying on the context cues has been successful on diverse benchmark datasets [51]. However, such monocular depth estimation methods [8, 50, 57] heavily rely on the specific prior knowledge of the scenes, objects, perspectives, and textures, and they may not generalize well to unseen data. Other cues, e.g., multi-view consistent feature cues [52, 64], can be used to improve the generalization of depth estimation.

The other powerful but under-explored cue for depth estimation is the *focus/defocus* information [22, 58, 59], where the depth can be reflected as the sharpness degree of the image, as a function of focal distances [32]. Depth estimation from focus/defocus is to predict the depth map from a *focal stack* of the scene, which is a set of images captured by a camera focused on different focal planes [31]. Depth estimation from the focal stack can be traced back to the depth of field control problem [5], capturing focal stack images using a light field camera [25]. Conventional methods [3, 15, 27] tackle this with handcrafted features that depend on pixel sharpness. However, these methods often fail in some textureless scenes. To extract more informative features for this task, Convolutional Neural Networks (CNNs) have been exploited to learn to predict the depth map from the focal stack [9, 10, 13, 28, 53, 58, 59, 61]. DDFNet [9], AiFDepthNet [13], and DFVNet [10] leverage the in-focus cues to estimate depth. DefocusNet [32] attempts to learn the permutation invariant defocus cues, also referred to as Circle-of-Confusion (CoC). These methods employ 2D or 3D convolutions to represent the visual and focal features across the spatial domain and stack channels. They fuse the stacked network 2D depth outputs [32] or predict a single 2D depth map from the 3D feature volume [10]. Although CNNs' receptive fields can be enlarged with the increase of the network depth, these CNN-based models are restricted to capturing the features in local areas. Moreover, existing methods are constrained to the focal stack with a constant

number of images during the training and testing. It is hard to generalize to stacks with an arbitrary number of images.

In this paper, we propose a novel Transformer-based network for depth estimation from focal stacks, which is referred to as FocDepthFormer in Figure 1. The core component of FocDepthFormer is a module of *Transformer with LSTM*, which consists of a Transformer encoder [48], an LSTM-based recurrent module [45] applied to the latent tokens, and a CNN decoder. The Transformer and LSTM are used to separately model the spatial and stack information. Different from the CNNs [10] restricted to local representation, the Transformer encoder captures the visual features by a larger receptive field. The self-attention mechanism in vision Transformer (ViT) [48] empowers the *cross reference* among the non-local patterns, allowing the Transformer encoder to capture more informative features to represent the sharpness and blur characteristics. Considering that the focal stacks may have arbitrary and unknown numbers of images, we use the LSTM in latent feature space to fuse the focusing information in the whole stack for depth prediction. It differs from the existing focal stack depth estimation methods [10, 13, 32], and the monocular depth estimation methods based on CNNs or Transformers [23, 33], which only focus on handling the input with a constant number of images. Specifically, we fuse the activated token features via the recurrent LSTM module after the Transformer encoder in a compact way. The design enables the proposed model to handle arbitrary lengths of focal stacks with a pre-defined order in training and testing, with higher flexibility in practice. Before feeding the input into the Transformer, we apply an early-stage convolutional encoder with multi-scale kernels [38] to directly capture the low-level focus/defocus features at multi-scale. Considering the limited focal stack data available, our model can further leverage monocular depth estimation datasets to pre-train the visual feature representation of FocDepthFormer, thanks to the flexibility of taking varying number of input images from the recurrent module LSTM. The main contributions of this work can be summarized as,

- We propose a novel Transformer-based network model for depth estimation from focal stack images. It uses a vision Transformer encoder with self-attention to capture the non-local spatial visual features for representing the sharpness and blur patterns. An LSTM-based recurrent module is used to integrate the stack features, enabling the model to handle an arbitrary number of input images. Relying on this structure, we can pre-train the model with a monocular depth estimation dataset flexibly, to alleviate the demands for focal stack data, which is limited and costly to collect.
- Specifically, we propose to use multi-scale kernels to directly capture the low-level focus/defocus features at multi-scale, in an early-stage convolutional encoder. For

LSTM, we use a grouping operation to control the recurrent complexity and memory footprint over tokens without scaling complexity when the token number is big. This is achieved by applying the LSTM merely on a fraction of embedding tokens while preserving information on other non-activated tokens by taking the average.

- We conduct a comprehensive ablation test qualitatively and quantitatively to justify the merits of using attention for capturing focus/defocus features, along with the benefits brought by the recurrent LSTM in latent token space.

2. Related work

Depth from focus. Depth estimation from focal stacks utilizes the relative sharpness in the stack images for depth prediction. Several traditional machine learning methods [15, 27, 31] view this problem as an image filtering and stitching process. Johannsen *et al.* [60] summarizes the methods developed so far on solving the challenging issues of light field cameras, which has created a base in this research direction. Recently, CNN-based methods have been developed to address focal stacks. DDFF-Net [9] proposes the first end-to-end learning model to train on the released DDFF 12-Scene dataset. DFVNet [10] employs the first-order derivative of the volume features in the stack. AiFNet [13] aims to bridge the gap between the supervised and unsupervised methods with or without ground truth depth. Barratt *et al.* [22] formulate this problem as an inverse optimization problem, where the gradient descent search is applied to recovering an all-in-focus image and depth map simultaneously. DefocusNet [32] exploits the Circle-of-Confusion, a defocus cue determined by focal plane depth, to generate the intermediate defocus maps for the final depth estimation. Saeed Anwar *et al.* [61] leverage defocus cues to recover the all-in-focus images by removing the blur of a single image. Gur and Wolf [53] present the depth estimation from a single image by leveraging the defocus cues to infer the disparity at varying viewpoints.

Attention-based models. The success of attention-based models [12] in sequential tasks has motivated the rise of Vision Transformer for computer vision tasks. The Vision Transformer represents the input images into a series of patches (16×16). Although this model performs favorably against the CNN-based models for image recognition, a recent study [38] shows that injecting a small convolutional inductive bias as early kernels dramatically increases the performance and stability of the Transformer encoder. Regarding the depth estimation task, Ranftl *et al.* [33] employ a Transformer-based model as the backbone to generate tokens from images, and tokens are assembled into an image-like representation at multi-scale. DepthFormer [23] merge tokens at different layer levels to improve the depth estimation performance. The most recent breakthrough in this area, Swin Transformer [55] achieves a larger recep-

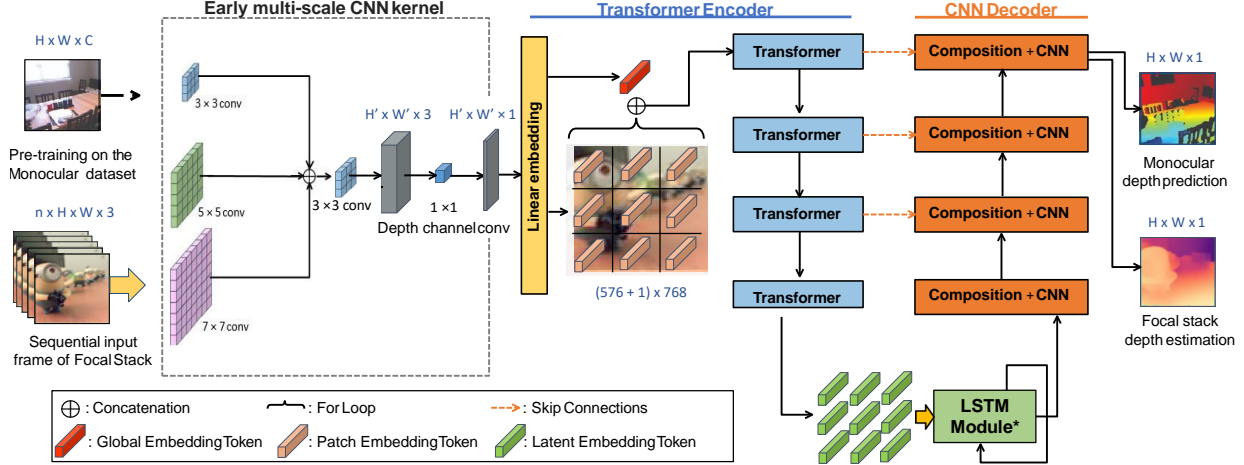


Figure 1. The overview of our proposed network, FocDepthFormer, presented with the core components, the Transformer encoder, the recurrent LSTM module, and the CNN decoder. The early-stage multi-scale convolutional kernels preceding the Transformer encoder are presented under the dashed line. The multi-scale feature maps are concatenated and then go through convolution over the image spatially and along the feature depth channel subsequently. Finally, the fused feature map is split into patches, and projected patch-wisely by linear embedding layer into tokens. The red token represents a global embedding token mapped from the whole image and is summed with each individual patch embedding token respectively.

tive field by shifting the attention window, which unveils the promising potential of the Transformer model.

Recurrent networks. Recurrent networks, specifically LSTM [45], have been successful in modeling temporal distributions for tracking [43], and segmentation [42] of videos. The use of LSTM is without too much computational overhead, as demonstrated in SliceNet [16] by fusion of multi-scale features for depth estimation from a panoramic image. Recent works [41, 44] combine LSTM with Transformer for language understanding, this has given the networks long-range temporal attention.

3. The proposed method

3.1. Overview

Given a focal stack, \mathbf{S} of n images ordered by the focus distances from near to far, *i.e.*, $\mathbf{S} = (\mathbf{x}_i)_{i=1}^n$, where each image $\mathbf{x} \in \mathbb{R}^{H \times W \times 3}$, our goal is to generate a single depth map $\mathbf{D} \in \mathbb{R}^{H \times W \times 1}$ from it. Unlike the vanilla Transformer [48], the image \mathbf{x} is first encoded by an *early-stage multi-scale kernel-based convolution* $\mathcal{F}(\cdot)$. This ensures a multi-scale feature representation \mathbf{x}' of focal stack images. Next, the *transformer encoder* $g(\cdot)$ represents the feature maps into a series of ordered tokens sharing information by self-attention. It differentiates between the in-focus features and blur features, to encode spatial features from each image input. The *recurrent LSTM module* takes the cached latent tokens sequentially from different frames as inputs and fuses them along the stack. This fusion process is learned in the latent space by LSTM. Our design with LSTMs extends the model capability to an arbitrary number of image inputs.

The final disparity map is decoded by CNNs $d(\cdot)$ from the aggregated tokens of all stack images.

3.2. Early-stage encoding with multi-scale kernels

To capture the low-level focus/defocus features at different scales, we apply an early-stage convolutional encoder with multi-scale kernels, which is different from the method using a single kernel size-based convolution stem before Transformer [38]. As shown in Figure 1, the early-stage encoder uses three conv kernels to generate multi-scale feature maps $f_m(\mathbf{x})$, $\{m = 1, 2, 3\}$. All the feature maps are concatenated and merged into feature map $\mathbf{x}' \in \mathbb{R}^{H' \times W' \times 1}$ via spatial conv first, followed by 1×1 conv on depth channel,

$$\mathbf{x}' = \mathcal{F}(\mathbf{x}) = \text{Conv}(\text{Concat}(f_m(\mathbf{x}))), \quad (1)$$

where m is index from 1 to 3. The feature concatenation after convolutions by four kernel sizes preserves fine-grained details of the sharp features at varying depth scales. The first module from left in Figure 1), composed of multi-scale kernel convolution in parallel followed by the sequential convolution, can guarantee the model to be featured with a large receptive field beyond the 7×7 kernel size to capture more defocus cues while preserving more sharp details. More implementation details can be found in the Appendix.

3.3. Transformer with LSTM

Transformer encoder. The Transformer encoder in Figure 1, $g(\cdot)$ takes the feature maps \mathbf{x}' from the early-stage multi-scale convolutions to generate a series of tokens $(\mathbf{t}'_p)_{p=1}^k$,

$$\mathbf{t}'_1, \mathbf{t}'_2, \dots, \mathbf{t}'_k = g(\mathbf{x}'). \quad (2)$$

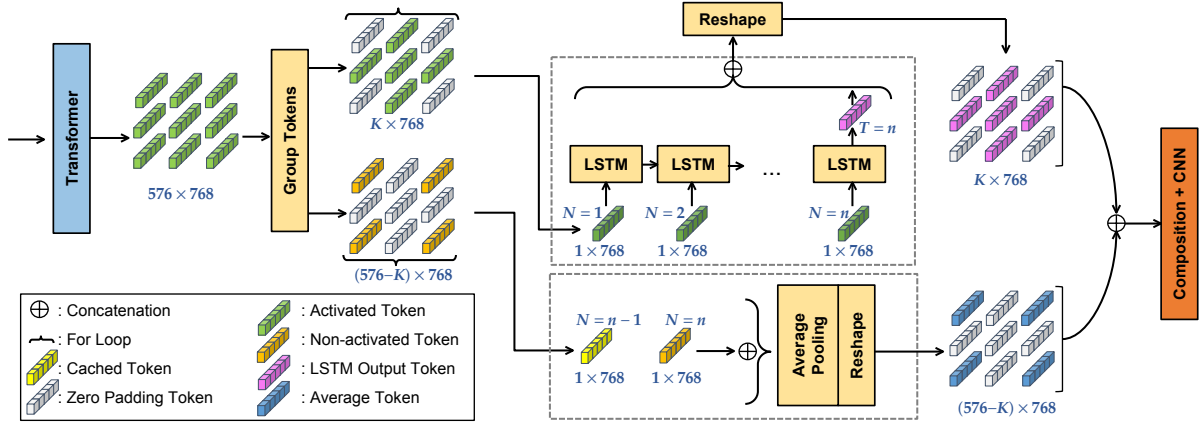


Figure 2. To unfold the LSTM module of our network, first, the output tokens from the Transformer encoder are grouped into activated and non-activated tokens, and subsequently processed by recurrent LSTMs or average pooling, respectively. After that, the output tokens are reshaped and concatenated before delivering to the CNN decoder to predict the depth disparity map.

Specifically, the Transformer encoder employs a linear embedding layer, that divides the input feature maps \mathbf{x}' from the conv encoder into k patches of size 16×16 , *i.e.*, $\mathbf{x}'_p \in \mathbf{x}'$, $p = 1, 2, \dots, k$ is projected by linear embedding layer (MLP) into the corresponding embedding tokens, $(\mathbf{l}_p)_{p=1}^k$, and each token in 768-dim (576 in total). The Transformer *Position Embedding* to encode the position information of the image patches in an iterative order. An MLP layer generates the Global Embedding Token (Figure 1), by mapping the whole image into a global token, then adding each individual patch embedding token. Every linear embedding token is projected via weight matrix $\mathbf{W}^{(\cdot)}$ from dimension d_m into three vectors, the Query, \mathbf{l}_Q , the Key, \mathbf{l}_K and the Value, \mathbf{l}_V with dimensions d_Q , d_K , and d_V respectively. The Queries, Keys, and Values go through the Multi-Head-Attention (MHA) units in parallel,

$$\text{MHA}(\mathbf{l}_Q, \mathbf{l}_K, \mathbf{l}_V) = (\text{head}_1 \oplus \dots \oplus \text{head}_N) \mathbf{W}^O, \quad (3)$$

$$\text{head}_i = \text{softmax}\left(\frac{\mathbf{l}_Q \mathbf{W}^{1_Q} \mathbf{l}_K \mathbf{W}^{1_K}}{\sqrt{d_k}}\right) \mathbf{l}_V \mathbf{W}^{1_V}, \quad (4)$$

where $\mathbf{W}^{1_Q} \in \mathbb{R}^{d_m \times d_V}$, $\mathbf{W}_i^{1_K} \in \mathbb{R}^{d_m \times d_K}$, $\mathbf{W}^{1_V} \in \mathbb{R}^{d_m \times d_V}$, and $\mathbf{W}^O \in \mathbb{R}^{d_m \times d_V}$. the tokens after the Multi-Head-Attention modules, $(\mathbf{t}'_p)_{p=1}^k$ can encode features to differentiate between the focus and defocus cues from different stack image patches at the same image spatial location, as demonstrated in Figure 3. As a result, the more in-focus sharp features of the image patches are attended more in embedding space, or vice versa.

LSTM module. To enable the model to flexibly handle stacks with arbitrary lengths (instead of fixed length in existing methods [9, 10, 13]), we use an LSTM to fuse the sharp features along the stack incrementally. LSTM considers the patch embedding tokens at the same image position as sequential features along the stack dimension. The corresponding feature tokens $(\mathbf{t}'_p)_{p=1}^k$ from stack images at

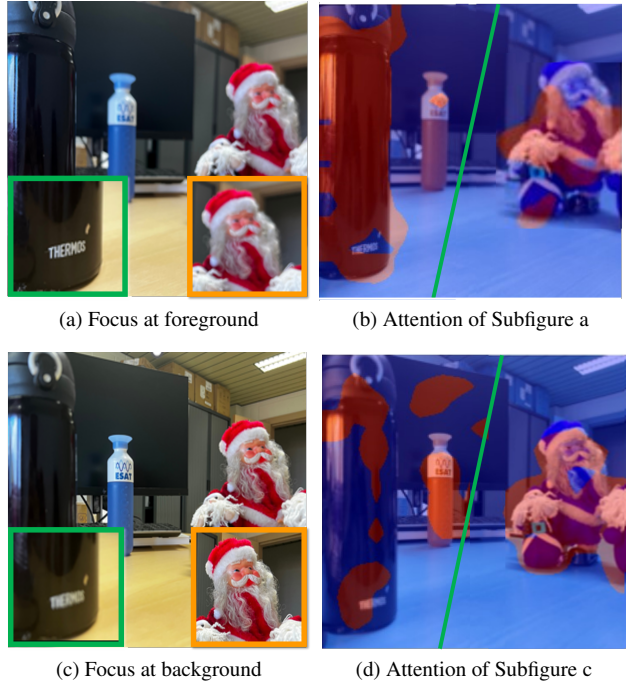


Figure 3. The Transformer attention comparisons on the image input (left column). We crop image patches (in green and orange boxes) at the same locations in (a) and (c) to calculate the self-attention map for other locations. In (b) and (d), the attention map on the left of the green line and right of the green line are the attention output of the green and orange box, respectively. It shows that the patches can attend to the fore- and background areas with related focus and defocus characteristics.

time step n are ordered spatially and fed into LSTM modules arranged in spatial image order accordingly. For each position, each LSTM module incrementally fuses the latent token \mathbf{t}'_p from a stack. It differs from the existing models that are restricted to a 3D volume stack with a pre-defined and fixed size [9, 10, 13]. In practice, this sequential pro-

cessing in the latent space of the focal stack will not result in too much time complexity, as shown in Sec. 4.1).

Before the LSTM modules, the tokens of image patches of one frame are categorized as activated tokens and non-activated tokens to represent the informative level of the features. L_2 norm $\|\cdot\|$ of each embedding token is compared with a threshold 0.4, as shown in Figure 2. For tokens of a single frame, only the activated tokens are fed into the LSTM. This operation can mitigate the computational complexity of using LSTM by applying the operation over a fraction of latent tokens only:

$$\mathbf{t}_p^n = LSTM(\mathbf{t}_p^n, \mathbf{h}_p^{n-1}, c^n), \quad (5)$$

where $p = 1, 2, \dots, k_1$, and n is the number of focal stack images. We set the number of hidden layers of LSTM to be 10. c is the memory cell updated continuously at each step by input \mathbf{t}_p^n and hidden state \mathbf{h} . The non-activated tokens $(\mathbf{t}'_p)_{p=1}^{k-k_1}$ are averaged with the cached tokens of the last step corresponding to the same embedding position. Finally, two output token groups are arranged according to the input embedding order to generate the final tokens $(\mathbf{t}_p)_{p=1}^k$. **CNN decoder.** Our decoder $d(\cdot)$ is similar to the work by Ranftl *et al.* [33], using Transpose-conv to fuse feature maps after the LSTMs along with feature maps $g(\mathbf{x}')$ from encoder via skip connections, as shown in Figure 1, to predict the disparity map by $d(\cdot)$, and the reciprocal of disparity is scaled by multiplication of baseline b and focus distance f .

$$\hat{\mathbf{D}} = \frac{b \cdot f}{d((\mathbf{t}_p)_{p=1}^k, g_i(\mathbf{x}'))}, \quad i = \{1, 2, 3\}. \quad (6)$$

3.4. Training loss

Our training loss is composed of MSE loss plus a gradient loss \mathcal{L}_{Grad} weighted by a scalar α ,

$$\mathcal{L}_{total} = \mathcal{L}_{MSE}(\hat{\mathbf{D}}, \mathbf{D}) + \alpha \mathcal{L}_{Grad}(\nabla \hat{\mathbf{D}}, \nabla \mathbf{D}), \quad (7)$$

where \mathbf{D} is the ground truth depth, and $\hat{\mathbf{D}}$ as predicted depth, while the gradient is $\nabla_{xy} \mathbf{D} = (\nabla_x \mathbf{D}, \nabla_y \mathbf{D})$. The loss is calculated from the sum of pixel errors.

3.5. Pre-training with monocular depth estimation

The focal stack datasets are usually small due to the high cost and difficulty of data collection. To alleviate data shortage by fully exploring the potential of the Transformer, we can resort to pre-training of our Transformer encoder on common monocular depth estimation data, *e.g.*, NYUv2 dataset [34] to learn a better spatial representation. Benefiting from the LSTM-based design, the proposed model can take an arbitrary number of images as input and thus can naturally incorporate the prior from pre-training on the monocular dataset. Although the monocular depth dataset differs from the focal stack dataset, the pre-training can help

the model learn a universal visual representation for depth prediction. Despite the benefits gained from pre-training, our model can still achieve plausible results without the pre-training completely, as shown in the experiments below.

4. Experiments

4.1. Experimental settings

Datasets. We evaluate our network on four benchmark focal stack datasets: DDFF 12-Scene [9], Mobile Depth [17], LightField4D [14], and FOD500 [10]. Our model can be pre-trained on the monocular RGB-D dataset NYUv2 [34]. We trained our model on DDFF 12Scene and FOD500 respectively for the following experiments, while the other two datasets are utilized for the generalizability tests. Table 1 summarizes our evaluation datasets and their properties.

Dataset	Image source	GT type	Cause of defocus
DDFF 12-Scene [9]	Real	Depth	Light-field settings
Mobile Depth [17]	Real	—	Real
LightField4D [14]	Real	Disparity	Light-field settings
FOD500 [10]	Synthetic	Depth	Blendering

Table 1. Summary of evaluation datasets.

Implementation details. For evaluation on DDFF 12-Scene, we trained our model on DDFF 12-Scene with pre-training on NYUv2 [34] and without pre-training, and present the results of both. 16×16 patch size and 384×384 image size are used for Transformer. Our network employs an Adam optimizer with a learning rate of $1e-4$ and a momentum at 0.9. The regularization scalar α in Eq. (7) is set to 0.2. Regarding hardware setup, we use a single Nvidia RTX 2070 GPU with 8GB vRAM for all training and tests.

Metric evaluation. In this work, we perform the quantitative evaluation by using the following metrics: Root Mean Squared Error (RSME), logarithmic Root Mean Squared Error (logRSME), relative absolute error (absRel), relative squared error (sqrRel), bumpiness (bump), accuracy with a threshold at three levels (1.25 , 1.25^2 , and 1.25^3).

Runtime. We evaluate the runtime of the proposed method and baseline methods by running them on the focal stacks from DDFF 12-Scene. Our FocDepthFormer takes 15ms to sequentially process a stack with 10 images and 2ms on average per image. With the same setting, DDFFNet [9] takes 200ms for each stack, and DFVNet [10] with 20-30ms. More model complexity and computation analysis of our model and baseline models can be found in the supplementary part.

4.2. Comparisons to the state-of-the-art methods

DDFFNet [9] and DefocusNet [32] do not provide the pre-trained weights, so we used their open-source codes to train the networks from scratch. DefocusNet [32] has two architectures and the "PoolAE" architecture is selected for

Model	RMSE↓	logRMSE↓	absRel↓	sqrRel↓	Bump↓	$\delta \uparrow$	$\delta^2 \uparrow$	$\delta^3 \uparrow$
DDFFNet [9]	2.91e-2	0.320	0.293	1.2e-2	0.59	61.95	85.14	92.98
DefocusNet [32]	2.55e-2	0.230	0.180	6.0e-3	0.46	72.56	94.15	97.92
DFVNet [10]	2.13e-2	0.210	<u>0.171</u>	6.2e-3	0.32	76.74	94.23	98.14
AiFNet [13]	2.32e-2	0.290	0.251	8.3e-3	0.63	68.33	87.40	93.96
Ours (w/o Pre-training)	<u>2.01e-2</u>	<u>0.206</u>	0.173	<u>5.7e-3</u>	<u>0.26</u>	<u>78.01</u>	<u>95.04</u>	<u>98.32</u>
Ours (w/ Pre-training)	1.96e-2	0.197	0.161	5.4e-3	0.23	79.06	96.08	98.57

Table 2. Evaluation results on DDFF 12-Scene dataset. The best results are denoted in **Red** while **Blue** indicates the second-best. $\delta = 1.25$.

Model	RMSE↓	logRMSE↓	absRel↓	sqrRel↓	Bump↓	$\delta \uparrow$	$\delta^2 \uparrow$	$\delta^3 \uparrow$
DDFFNet [9]	0.167	0.271	0.172	3.56e-2	1.74	72.82	89.96	96.26
DefocusNet [32]	0.134	0.243	0.150	3.59e-2	1.57	81.14	93.31	96.62
DFVNet [10]	<u>0.129</u>	<u>0.210</u>	<u>0.131</u>	<u>2.39e-2</u>	<u>1.44</u>	81.90	<u>94.68</u>	<u>98.05</u>
AiFNet [13]	0.265	0.451	0.400	4.32e-1	2.13	<u>85.12</u>	91.11	93.12
Ours (w/o Pre-training)	0.121	0.203	0.129	2.36e-2	1.38	85.47	94.75	98.13

Table 3. Metric evaluation results on FOD500 test dataset. Here the first 400 FOD500 focal stacks are used for training, following the standard setting from DFVNet [10]. The best results are denoted in **Red**, while **Blue** indicates the second-best. $\delta = 1.25$.

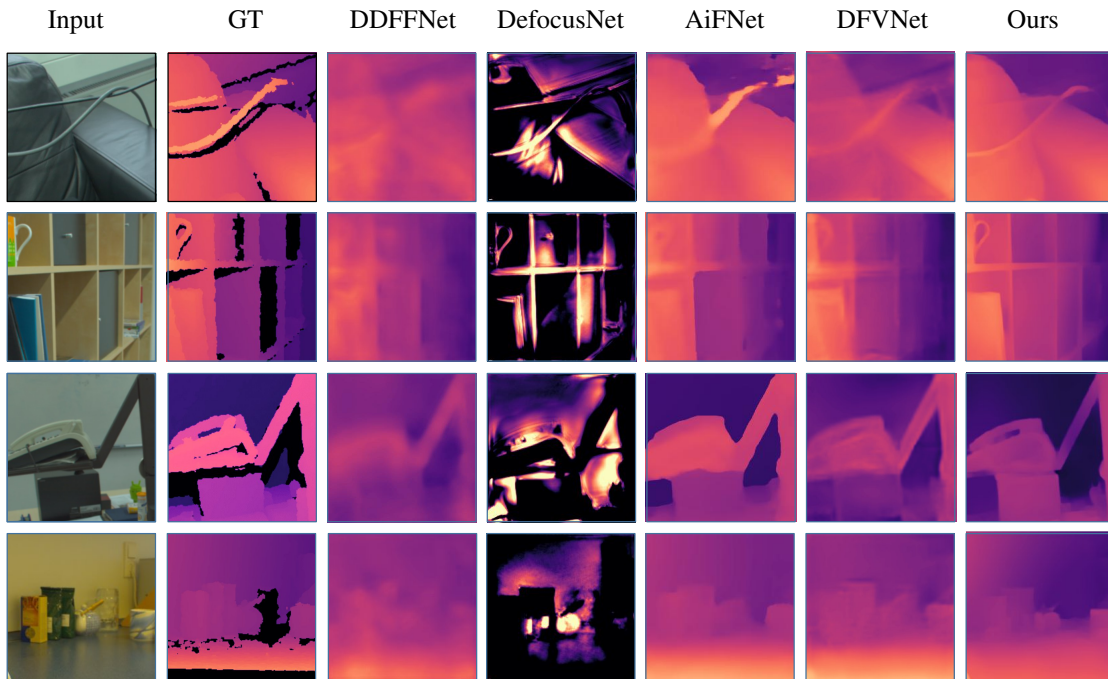


Figure 4. Qualitative evaluation of our model on DDFF 12-Scene dataset.

comparison because of its good average performance. For AiFNet [13], and DFVNet [10], their provided pre-trained weights are used to conduct the following tests.

Results on DDFF 12-Scene. Table 2 reports the quantitative evaluation results of our model on the DDFF 12-scene. Because the “test set” ground truth of DDFF-12 Scene is not publicly available, following the standard protocol in other compared works, we evaluate the models on “valida-

tion set”, following the same split provided by DDFFNet [9]. Furthermore, the proposed model trained on DDFF-12 can also perform well on other completely unseen datasets as follows, which validates the generalization ability (instead of over-fitting). The results in the table show that our model w/o pre-training outperforms the prior models on all the metrics except absRel compared to DFVNet, in particular, our model achieves an accuracy of 78.01% ($\delta = 1.25$),

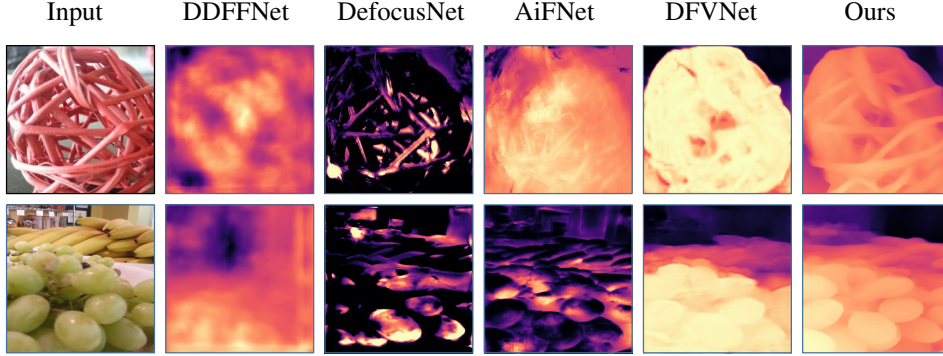


Figure 5. Qualitative evaluation of our model on Mobile Depth dataset.

an improvement of 1.27% over the model (DFVNet), and by Bumpiness metric value is a 0.26, one third less than DFVNet. We further show that our model achieves the highest accuracy of 78.01% ($\delta = 1.25$), with more than one percentile margin compared to the second-best baseline model, and this can be attributed to the compact design of Transformer and LSTM, learning spatial features and stack information separately and efficiently. Additionally, from the table, we can see that pre-training brings considerable beneficial margins across all metrics, in particular for absRel and Bump with an improvement of around 7% and 12% respectively over pure training of ours, revealing the potential of our model. Figure 4 depicts the qualitative results of our model on the DDFF 12-Scene. From the figure, decent depth estimation results of our model are witnessed, which preserves more fine-grained details visually, *i.e.*, details such as the thin wire hanging over the sofa (first row) and the cup handle on the shelf (second row). More sample results are available in supplementary materials.

Results on FOD500. Table 3 presents the quantitative evaluation of our model on the synthetic FOD500 dataset. We use the last 100 image stacks from the dataset as a test set to present results, while the first 400 image stacks are for training. DDFFNet and Defocus are re-trained on FOD500 from scratch respectively. The results indicate that our model achieves consistent superiority on all metrics compared to baselines. In experiments, we found that pre-training on NYUv2 brings no benefit due to the gap between synthetic data and real data. We also observed that the proposed method can achieve satisfactory and competitive results with only a few training epochs. The supplementary materials provide more qualitative results on FOD500.

4.3. Cross dataset evaluation

To validate the generalizability of our model, it is trained on DDFF 12-Scene, and then evaluated on Mobile Depth and LightField4D datasets. The Mobile Depth is a challenging focal stack dataset captured by a mobile phone camera including 11 aligned focal stacks of varying focal stack num-

bers without ground truth. Figure 5 demonstrates the results on this Mobile Depth. It can be observed that our model preserves sharp information for depth prediction from complex scenes, such as the ball with many holes (first row). In complex topological structures, *i.e.*, grape granules of our model outputs are quite recognizable. Moreover, our model can fuse a wide range of depth fields including backgrounds like bananas (second row). Additionally, Mobile Depth contains varying focal stack numbers per scene, the baseline methods cannot process directly the stack image number different from the training settings, but our model can handle this arbitrary number of inputs. For generalization tests on LightField4D, our model and other baseline models were pre-trained on DDFF 12-Scene only, except for AiFNet [13] which is also pre-trained on LightField4D all-in-focus color images in an unsupervised way. Figure 6 exhibits the visual results. The results demonstrate that predicted depth maps of our model are more accurate for complex objects compared to AiFNet [13]. Please refer to the supplementary part for quantitative results. All these test results show that our model achieves comparable generalization performance to prior models without training specifically on these focal stack datasets.

4.4. Ablation study

The following tests all use the DDFF 12-Scene validation set and omit the data name for brevity.

Transformer encoder: From Table 4, a comparison of Transformer and CNN-based encoder is presented, specifically, by using vanilla Transformer, Swin Transformer, and CNN-based DDFF-Net model. For fairness, we remove the early kernels of our model in experiments. The results indicate that the ViT-base Transformer achieves the highest accuracy in the setting, with approximately 33% improvement over the CNN-based DDFF-Net encoder on RMSE.

Multi-scale early-stage kernels: Table 5 compares various early CNN kernel design combinations with our Transformer encoder (ViT). The proposed *early-stage multi-scale kernels* encoder guarantees good performance, while ei-

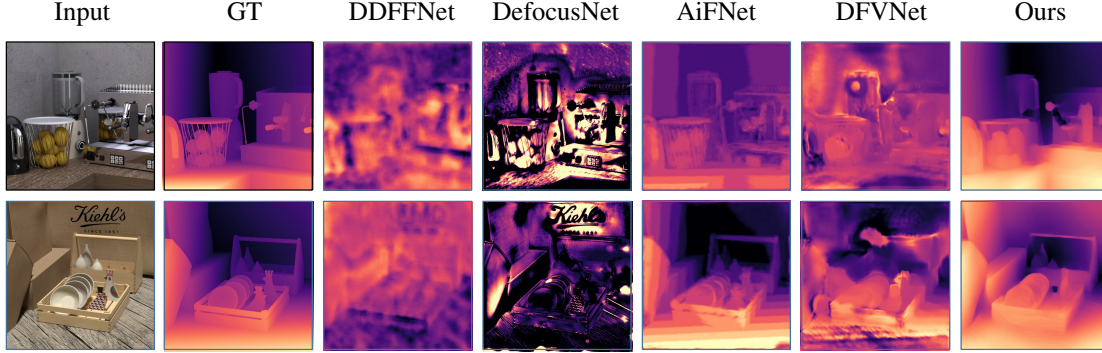


Figure 6. Qualitative evaluation of our model on LightField4D dataset.

	RMSE↓	absRel↓	Bump↓
ViT-base encoder	2.06e-2	0.197	0.29
Swin Transformer encoder	2.21e-2	0.205	0.32
CNN encoder	3.12e-2	0.268	0.46

Table 4. Metric evaluation of various encoders.

ther no multi-scale kernels or no subsequent convs after in-parallel convs degrades the model performance.

	RMSE↓	absRel↓	Bump↓
<i>multi-scale kernels w/ depth convs + ViT</i>	2.01e-2	0.173	0.26
Constant kernel size at 3×3 + ViT	2.18e-2	0.216	0.31
<i>multi-scale kernels w/o depth convs + ViT</i>	2.27e-2	0.229	0.29

Table 5. Results of different designs of the early-stage conv.

LSTM for handling arbitrary stack length: The proposed LSTM-based method can process the focal stack with arbitrary lengths different from the length of training stacks. The other designs restrict the input to a fixed length. We conduct experiments with DDFF 12-Scene data to show the benefits of the proposed LSTM-based model and report the RMSE comparison of our model and DFVNet in Table 6. We first use 10-frame (10F) stacks to train our model and DFVNet [10] (*i.e.*, Ours-10F and DFVNet-10F). During testing, DFVNet-10F cannot handle stacks with less than 10 frames. Instead, due to the fixed stack size requirements of the train and test, DFVNet has to be retrained respectively (DFVNet-#F), while our model is trained once on 10-frame stacks and tested directly at any number of stack images. The focal stack images are provided in an order of focus distances. Despite the model performance being inferior to DFVNet from the beginning, the learning performance of LSTM converges very fast after that.

Model	2 Frames	4 Frames	6 Frames	8 Frames	10 Frames
Ours-10F	3.2e-2	2.61e-2	2.18e-2	2.16e-2	2.04e-2
DFVNet-10F	—	—	—	—	2.43e-2
DFVNet-#F	2.97e-2	2.70e-2	2.52e-2	2.47e-2	2.43e-2

Table 6. RMSE for evaluation of LSTM compared to DFVNet.

Loss Function: Table 7 exhibits results of using three loss types, MSE, MAE, and Regularized MSE (MSE with gradient regularizer). It shows that the MSE loss can guaran-

tee a better performance compared to MAE. Moreover, the gradient regularizer helps us to achieve the best accuracy reflected by the bumpiness metric (0.24).

	RMSE↓	absRel↓	Bump↓
MSE loss	2.94e-2	0.280	0.50
MAE loss	3.76e-2	0.372	0.62
MSE + Gradient loss	2.01e-2	0.173	0.26

Table 7. Metric evaluation for our model with different losses.

Pre-training: Table 8 shows that the proposed method’s performance can be improved with pre-training, benefiting from the compact model design with Transformer and LSTM. Without pre-training, our model still achieves plausible and competitive results. Although DFVNet cannot directly use the monocular depth estimation data for pre-training, we try to apply pre-training for it by stacking the repeated monocular image of NYUv2 to form a stack in use. The pre-training can bring no improvement for DFVNet, and even can degrade the performance.

	Pre-training	RMSE↓	logRMSE↓	absRel↓	Bump↓
Ours	✗	2.01e-2	0.206	0.173	0.26
	✓	1.96e-2	0.197	0.161	0.19
DFVNet	✗	2.13e-2	0.210	0.171	0.32
	✓	2.57e-2	0.233	0.184	0.49

Table 8. Pre-training contribution comparisons.

5. Conclusion

We have presented FocDepthFormer model, to tackle the depth estimation from focal stack problem. The essential component of our network is a Transformer encoder with a recurrent LSTM module at latent space that enables the network to model spatial and stack information separately. our model can tackle varying focal stack lengths. For evaluation purposes, we have compared the proposed method to prior works on the public focal stack dataset. Our results demonstrate that the proposed model outperforms the prior models on multiple metrics across various focal stack benchmarks. Although the proposed method is efficient as discussed, the limitation of our model is the increased memory

footprint compared to simpler CNN-based methods, which are caused by Transformer and may be reduced via more efficient Transformer design techniques. We will further explore large kernel size effects on capturing defocus cues.

References

- [1] C. Godard, O. Mac Aodha, and G. J. Brostow. 'Un-supervised monocular depth estimation with left-right consistency.' In Proceedings of the IEEE conference on computer vision and pattern recognition, 2017, pp. 270–279. [1](#)
- [2] D. Eigen, C. Puhrsch, and R. Fergus, 'Depth map prediction from a single image using a multi-scale deep network', Advances in neural information processing systems, vol. 27, 2014.
- [3] M. Moeller, M. Benning, C. Schönlieb, and D. Cremers, 'Variational depth from focus reconstruction', IEEE Transactions on Image Processing, vol. 24, no. 12, pp. 5369–5378, 2015. [1](#)
- [4] J. Xie, R. Girshick, and A. Farhadi, 'Deep3d: Fully automatic 2d-to-3d video conversion with deep convolutional neural networks', in European conference on computer vision, 2016, pp. 842–857. [1](#)
- [5] A. P. Pentland, 'A new sense for depth of field', IEEE transactions on pattern analysis and machine intelligence, pp. 523–531, 1987. [1](#)
- [6] J. L. Schonberger and J.-M. Frahm, 'Structure-from-motion revisited', in Proceedings of the IEEE conference on computer vision and pattern recognition, 2016, pp. 4104–4113.
- [7] M. Ramamonjisoa, M. Firman, J. Watson, V. Lepetit, and D. Turmukhambetov, 'Single image depth prediction with wavelet decomposition', in Proceedings of the IEEE/CVF conference on computer vision and pattern recognition, 2021, pp. 11089–11098.
- [8] C. Godard, O. Mac Aodha, M. Firman, and G. J. Brostow, 'Digging into self-supervised monocular depth estimation', in Proceedings of the IEEE/CVF International Conference on Computer Vision, 2019, pp. 3828–3838. [1](#)
- [9] C. Hazirbas, S. G. Soyer, M. C. Staab, L. Leal-Taixé, and D. Cremers, 'Deep depth from focus', in Asian conference on computer vision, 2018, pp. 525–541. [1](#), [2](#), [4](#), [5](#), [6](#)
- [10] F. Yang, X. Huang, and Z. Zhou, 'Deep Depth from Focus with Differential Focus Volume', in Proceedings of the IEEE/CVF Conference on Computer Vision and Pattern Recognition, 2022, pp. 12642–12651. [1](#), [2](#), [4](#), [5](#), [6](#), [8](#)
- [11] L. Ruan, B. Chen, J. Li, and M.-L. Lam, 'Aifnet: All-in-focus image restoration network using a light field-based dataset', IEEE Transactions on Computational Imaging, vol. 7, pp. 675–688, 2021. [1](#)
- [12] A. Vaswani et al., 'Attention is all you need', Advances in neural information processing systems, vol. 30, 2017. [2](#)
- [13] N.-H. Wang et al., 'Bridging unsupervised and supervised depth from focus via all-in-focus supervision', in Proceedings of the IEEE/CVF International Conference on Computer Vision, 2021, pp. 12621–12631. [1](#), [2](#), [4](#), [6](#), [7](#)
- [14] K. Honauer, O. Johannsen, D. Kondermann, and B. Goldluecke, 'A dataset and evaluation methodology for depth estimation on 4D light fields', in Asian conference on computer vision, 2016, pp. 19–34. [5](#)
- [15] J. Surh, H.-G. Jeon, Y. Park, S. Im, H. Ha, and I. So Kweon, 'Noise robust depth from focus using a ring difference filter', in Proceedings of the IEEE Conference on Computer Vision and Pattern Recognition, 2017, pp. 6328–6337. [1](#), [2](#)
- [16] G. Pintore, M. Agus, E. Almansa, J. Schneider, and E. Gobbetti, 'Slicenet: deep dense depth estimation from a single indoor panorama using a slice-based representation', in Proceedings of the IEEE/CVF Conference on Computer Vision and Pattern Recognition, 2021, pp. 11536–11545. [3](#)
- [17] F. T. Benavides, A. Ignatov, and R. Timofte, 'PhoneDepth: A Dataset for Monocular Depth Estimation on Mobile Devices', in Proceedings of the IEEE/CVF Conference on Computer Vision and Pattern Recognition, 2022, pp. 3049–3056. [5](#)
- [18] D. E. Jacobs, J. Baek, and M. Levoy, 'Focal stack compositing for depth of field control', Stanford Computer Graphics Laboratory Technical Report, vol. 1, no. 1, p. 2012, 2012.
- [19] W. Li, G. Wang, X. Chen, X. Yin, and X. Hu, 'Blurring-effect-free CNN for optimization of structural edges in focus stacking', in 2019 IEEE International Conference on Image Processing (ICIP), 2019, pp. 4634–4638.
- [20] H. Lin, C. Chen, S. B. Kang, and J. Yu, 'Depth recovery from light field using focal stack symmetry', in Proceedings of the IEEE International Conference on Computer Vision, 2015, pp. 3451–3459.
- [21] X. Kang, S. Yin, and Y. Fen, '3D reconstruction & assessment framework based on affordable 2D Lidar', in 2018 IEEE/ASME International Conference on Advanced Intelligent Mechatronics (AIM), 2018, pp. 292–297. [1](#)
- [22] S. Barratt and B. Hannel, 'Extracting the Depth and All-In-Focus Image from a Focal Stack', in Proceedings of the IEEE International Conference on Computer Vision, 2015, pp. 3451–3459. [1](#), [2](#)
- [23] A. Agarwal and C. Arora, 'Depthformer: Multiscale Vision Transformer For Monocular Depth Estima-

- tion With Local Global Information Fusion’, arXiv preprint arXiv:2207.04535, 2022. 2
- [24] J. Hornauer and V. Belagiannis, ‘Gradient-based Uncertainty for Monocular Depth Estimation’, in European Conference on Computer Vision, 2022, pp. 613–630.
- [25] C. Liu, J. Qiu, and M. Jiang, ‘Light field reconstruction from focal stack based on Landweber iterative scheme’, in Mathematics in Imaging, 2017, pp. MM2C-3. 1
- [26] S. M. H. Miangoleh, S. Dille, L. Mai, S. Paris, and Y. Aksoy, ‘Boosting monocular depth estimation models to high-resolution via content-adaptive multi-resolution merging’, in Proceedings of the IEEE Conference on Computer Vision and Pattern Recognition, 2021, pp. 9685–9694.
- [27] S. Suwajanakorn, C. Hernandez, and S. M. Seitz, ‘Depth from focus with your mobile phone’, in Proceedings of the IEEE Conference on Computer Vision and Pattern Recognition, 2015, pp. 3497–3506. 1, 2
- [28] R. He, H. Hong, B. Fu, and F. Liu, ‘Multi-task Learning for Monocular Depth and Defocus Estimations with Real Images’, arXiv preprint arXiv:2208.09848, 2022. 1
- [29] X. Yin, G. Wang, W. Li, and Q. Liao, ‘Large aperture focus stacking with max-gradient flow by anchored rolling filtering’, Applied optics, vol. 55, no. 20, pp. 5304–5309, 2016.
- [30] W. Li, G. Wang, X. Hu, and H. Yang, ‘Scene-adaptive image acquisition for focus stacking’, in 2018 25th IEEE International Conference on Image Processing (ICIP), 2018, pp. 1887–1891.
- [31] Y. Xiong and S. A. Shafer, ‘Depth from focusing and defocusing’, in Proceedings of IEEE Conference on Computer Vision and Pattern Recognition, 1993, pp. 68–73. 1, 2
- [32] M. Maximov, K. Galim, and L. Leal-Taixé, ‘Focus on defocus: bridging the synthetic to real domain gap for depth estimation’, in Proceedings of the IEEE/CVF Conference on Computer Vision and Pattern Recognition, 2020, pp. 1071–1080. 1, 2, 5, 6
- [33] R. Ranftl, A. Bochkovskiy, and V. Koltun, ‘Vision transformers for dense prediction’, in Proceedings of the IEEE/CVF International Conference on Computer Vision, 2021, pp. 12179–12188. 2, 5
- [34] N. Silberman, D. Hoiem, P. Kohli, and R. Fergus, ‘Indoor segmentation and support inference from rgb-d images’, in European conference on computer vision, 2012, pp. 746–760. 5
- [35] J. Cho, D. Min, Y. Kim, and K. Sohn, ‘DIML/CVL RGB-D dataset: 2M RGB-D images of natural indoor and outdoor scenes’, arXiv preprint arXiv:2110.11590, 2021.
- [36] R. Ranftl, K. Lasinger, D. Hafner, K. Schindler, and V. Koltun, ‘Towards Robust Monocular Depth Estimation: Mixing Datasets for Zero-shot Cross-dataset Transfer’, IEEE Transactions on Pattern Analysis and Machine Intelligence (TPAMI), 2020.
- [37] C. Godard, O. Mac Aodha, M. Firman, and G. J. Brostow, ‘Digging into Self-Supervised Monocular Depth Prediction’, The International Conference on Computer Vision (ICCV), Oct. 2019.
- [38] T. Xiao, M. Singh, E. Mintun, T. Darrell, P. Dollár, and R. Girshick, ‘Early convolutions help transformers see better’, Advances in Neural Information Processing Systems, vol. 34, pp. 30392–30400, 2021. 2, 3
- [39] H. Zhao, J. Shi, X. Qi, X. Wang, and J. Jia, ‘Pyramid scene parsing network’, in Proceedings of the IEEE conference on computer vision and pattern recognition, 2017, pp. 2881–2890.
- [40] O. Ronneberger, P. Fischer, and T. Brox, ‘U-net: Convolutional networks for biomedical image segmentation’, in International Conference on Medical image computing and computer-assisted intervention, 2015, pp. 234–241.
- [41] D. Hutchins, I. Schlag, Y. Wu, E. Dyer, and B. Neyshabur, ‘Block-recurrent transformers’, arXiv preprint arXiv:2203.07852, 2022. 3
- [42] N. Xu et al., ‘Youtube-vos: Sequence-to-sequence video object segmentation’, in Proceedings of the European conference on computer vision (ECCV), 2018, pp. 585–601. 3
- [43] C. I. Nwoye, D. Mutter, J. Marescaux, and N. Padoy, ‘Weakly supervised convolutional LSTM approach for tool tracking in laparoscopic videos’, International journal of computer assisted radiology and surgery, vol. 14, no. 6, pp. 1059–1067, 2019. 3
- [44] Z. Huang, P. Xu, D. Liang, A. Mishra, and B. Xiang, ‘TRANS-BLSTM: Transformer with bidirectional LSTM for language understanding’, arXiv preprint arXiv:2003.07000, 2020. 3
- [45] S. Hochreiter and J. Schmidhuber, ‘Long short-term memory’, Neural computation, vol. 9, no. 8, pp. 1735–1780, 1997. 2, 3
- [46] J. Hu, M. Ozay, Y. Zhang, and T. Okatani, ‘Revisiting single image depth estimation: Toward higher resolution maps with accurate object boundaries’, in 2019 IEEE Winter Conference on Applications of Computer Vision (WACV), 2019, pp. 1043–1051.
- [47] S. Anwar, Z. Hayder, and F. Porikli, ‘Depth Estimation and Blur Removal from a Single Out-of-focus Image’, in BMVC, 2017, vol. 1, p. 2.
- [48] A. Dosovitskiy *et al.*, ‘An Image is Worth 16x16 Words: Transformers for Image Recognition at Scale’, ICLR, 2021. 2, 3

- [49] F. Khan, S. Hussain, S. Basak, M. Moustafa, and P. Corcoran, ‘A Review of Benchmark Datasets and Training Loss Functions in Neural Depth Estimation’, *IEEE Access*, vol. 9, pp. 148479–148503, 2021.
- [50] X. Meng, C. Fan, Y. Ming, and H. Yu, ‘COR-Net: Context-based Ordinal Regression Network for Monocular Depth Estimation’, *IEEE Transactions on Circuits and Systems for Video Technology*, 2021. [1](#)
- [51] A. Geiger, P. Lenz, and R. Urtasun, ‘Are we ready for autonomous driving? the kitti vision benchmark suite’, in 2012 IEEE conference on computer vision and pattern recognition, 2012, pp. 3354–3361. [1](#)
- [52] G. Bae, I. Budvytis, and R. Cipolla, ‘Multi-View Depth Estimation by Fusing Single-View Depth Probability with Multi-View Geometry’, in *Proceedings of the IEEE/CVF Conference on Computer Vision and Pattern Recognition*, 2022, pp. 2842–2851. [1](#)
- [53] S. Gur and L. Wolf, ‘Single image depth estimation trained via depth from defocus cues’, in *Proceedings of the IEEE/CVF Conference on Computer Vision and Pattern Recognition*, 2019, pp. 7683–7692. [1](#), [2](#)
- [54] X. Kang, A. Herrera, H. Lema, E. Valencia, and P. Vandewalle, ‘Adaptive Sampling-based Particle Filter for Visual-inertial Gimbal in the Wild’, in 2023 IEEE International Conference on Robotics and Automation (ICRA), 2023, pp. 2738–2744. [1](#)
- [55] Z. Liu *et al.*, ‘Swin transformer: Hierarchical vision transformer using shifted windows’, in *Proceedings of the IEEE/CVF International Conference on Computer Vision*, 2021, pp. 10012–10022. [2](#)
- [56] R. Mahjourian, M. Wicke, and A. Angelova, ‘Unsupervised learning of depth and ego-motion from monocular video using 3d geometric constraints’, in *Proceedings of the IEEE conference on computer vision and pattern recognition*, 2018, pp. 5667–5675. [1](#)
- [57] A. Gordon, H. Li, R. Jonschkowski, and A. Angelova, ‘Depth from videos in the wild: Unsupervised monocular depth learning from unknown cameras’, in *Proceedings of the IEEE/CVF International Conference on Computer Vision*, 2019, pp. 8977–8986. [1](#)
- [58] H. Tang, S. Cohen, B. Price, S. Schiller, and K. N. Kutulakos, ‘Depth from defocus in the wild’, in *Proceedings of the IEEE/CVF Conference on Computer Vision and Pattern Recognition*, 2017, pp. 2740–2748. [1](#)
- [59] M. Carvalho, B. Le Saux, P. Trouvé-Peloux, A. Almansa, and F. Champagnat, ‘Deep Depth from Defocus: how can defocus blur improve 3D estimation using dense neural networks?’, in *Proceedings of the European Conference on Computer Vision (ECCV) Workshops*, 2018, pp. 0–0. [1](#)
- [60] O. Johannsen *et al.*, ‘A taxonomy and evaluation of dense light field depth estimation algorithms’, in *Proceedings of the IEEE Conference on Computer Vision and Pattern Recognition Workshops*, 2017, pp. 82–99. [2](#)
- [61] S. Anwar, Z. Hayder, and F. Porikli, ‘Deblur and deep depth from single defocus image’, *Machine vision and applications*, vol. 32, no. 1, pp. 1–13, 2021. [1](#), [2](#)
- [62] X. Kang, S. Yin, and Y. Fen, ‘3D reconstruction & assessment framework based on affordable 2D Lidar’, in 2018 IEEE/ASME International Conference on Advanced Intelligent Mechatronics (AIM), 2018, pp. 292–297. [1](#)
- [63] F. Zhang, V. Prisacariu, R. Yang, and P. H. S. Torr, ‘Ga-net: Guided aggregation net for end-to-end stereo matching’, in *Proceedings of the IEEE/CVF Conference on Computer Vision and Pattern Recognition*, 2019, pp. 185–194. [1](#)
- [64] N. Smolyanskiy, A. Kamenev, and S. Birchfield, ‘On the importance of stereo for accurate depth estimation: An efficient semi-supervised deep neural network approach’, in *Proceedings of the IEEE conference on computer vision and pattern recognition workshops*, 2018, pp. 1007–1015. [1](#)
- [65] X. Guo, H. Li, S. Yi, J. Ren, and X. Wang, ‘Learning monocular depth by distilling cross-domain stereo networks’, in *Proceedings of the European Conference on Computer Vision (ECCV)*, 2018, pp. 484–500. [1](#)
- [66] W. Yin, Y. Liu, C. Shen, and Y. Yan, ‘Enforcing geometric constraints of virtual normal for depth prediction’, in *Proceedings of the IEEE/CVF International Conference on Computer Vision*, 2019, pp. 5684–5693. [1](#)

FocDepthFormer: Transformer with LSTM for Depth Estimation from Focus

Supplementary Material

6. Focal principles

In the paper we present the features of our network model, a primary factor to explain our favorable results is the good identification ability of pixel sharpness, as mentioned in our paper. Usually, the sharpness of pixels can be evaluated according to the Circle-of-Confusion, C (in Fig. 7), defined as follows,

$$C = \frac{f^2}{N(z - d_f)} \left| 1 - \frac{d_f}{z} \right|, \quad (8)$$

where, N denotes f -number, as a ratio of focal length to the valid aperture diameter. C is the Circle of Confusion (CoC) diameter. d_f is the focus distance of the lens. z represents the distance from the lens to the target object. In general, the range of z is $[0, \infty]$. However, in reality, the range is always constrained by lower and upper bounds.

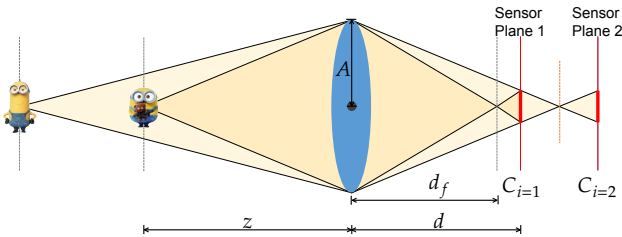


Figure 7. The rays emitted from an object placed at an axial distance z to the lens, converging at a distance d_f behind the lens. Sensor is situated at a distance d from focal lens. The pixels are sharply imaged when the sensor is placed right at focus distance, C is the CoC, that grows as the sensor position is deviated from the focus plane.

In Eq. 8, C is zero (C^*) when the image pixel is in-focus, and it is a signed value, where $C > 0$ indicates the camera focused in front of the sensor plane, while $C < 0$ is the reverse case, with camera focused behind the sensor plane. It can be inferred from the denominator, CoC C has two divergence points, at 0 and d_f respectively. Our model actually learn the mapping relationship from CoC to depth autonomously.

7. Metrics

The metrics used in our work for quantitative evaluations, are defined as follows,

$$RMSE : \sqrt{\frac{1}{|M|} \sum_{p \in \mathbf{x}} \|f(\mathbf{x}) - \mathbf{D}\|^2}, \quad (9)$$

$$\log RMSE : \sqrt{\frac{1}{|M|} \sum_{p \in \mathbf{x}} \|\log f(\mathbf{x}) - \mathbf{D}\|^2}, \quad (10)$$

$$absRel : \frac{1}{|M|} \sum_{p \in \mathbf{x}} \frac{|f(\mathbf{x}) - \mathbf{D}|}{\mathbf{D}}, \quad (11)$$

$$sqrRel : \frac{1}{|M|} \sum_{p \in M} \frac{\|f(\mathbf{x}) - \mathbf{D}\|}{\mathbf{D}}, \quad (12)$$

$$Bump : \frac{1}{|M|} \sum_{p \in \mathbf{x}} \min(0.05, \|\mathbf{H}_\Delta(p)\|) \times 100, \quad (13)$$

$$Accuracy(\delta) : \max\left(\frac{f(\mathbf{x})}{\mathbf{D}}, \frac{\mathbf{D}}{f(\mathbf{x})}\right) = \delta < threshold, \quad (14)$$

% of \mathbf{D} ,

where $\Delta = f(\mathbf{x}) - \mathbf{D}$ and \mathbf{H} is the Hessian matrix.

8. Effects of focal stack size

We perform extensive experiments to observe the effects of our model on various focal stack sizes. Fig. 8 shows the findings of our experiments on a focal stack from the DDFD 12-Scene validation set, with multiple objects placed at varying depths. In the figure, we plot RMSE and accuracy (in percentage) ($\delta = 1.25$) w.r.t. the number of focal stack images. We observe that the model accuracy increases with more input images from the focal stack in use, while the RMSE decreases correspondingly. Our model achieves a decent performance by six frames from a focal stack, which already captures good spatial and stack dimension information for depth cue estimation usually after 6 frames in use.

9. Attention map

From the comparison figures, it is obvious that the attention of the Transformer module can attend to more in-focus feature information, *i.e.*, the toy on the right side of Subfig. (d) is with higher attention compared to Subfig. (b) at the same location. It shows that the patches can attend to the fore- and background regions with related focus and defocus cues of corresponding depth field quite well. It further

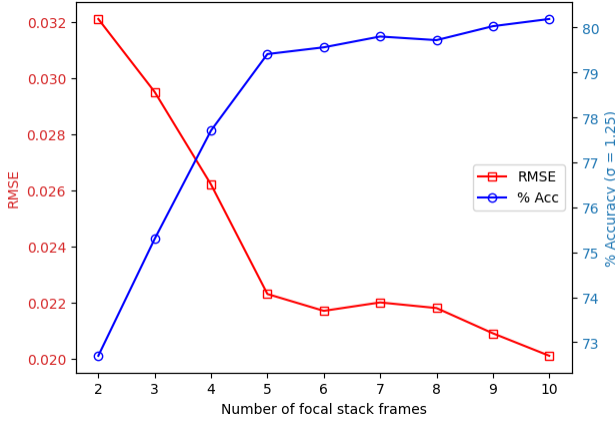


Figure 8. Our model performance w.r.t. the frame size of one focal stack sample from DDFD 12-Scene test.

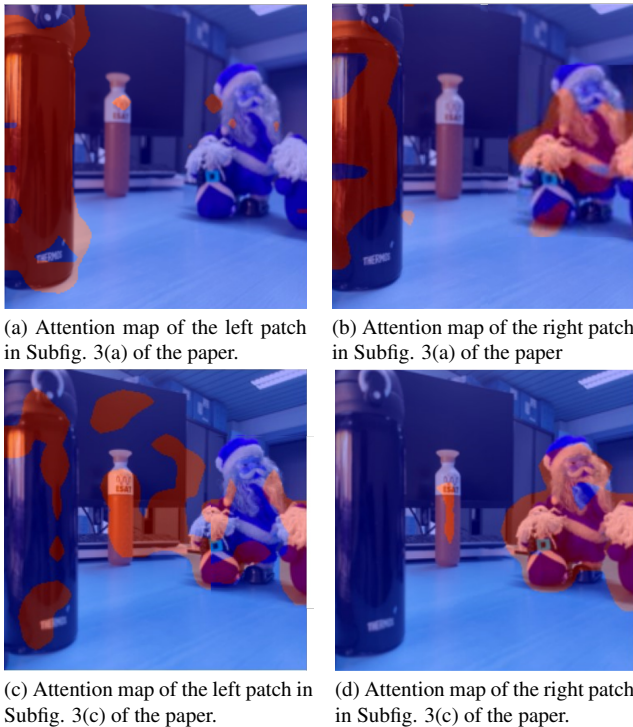


Figure 9. These subfigures are used as complementary materials to Fig. 3 of the paper, in order to show the complete Transformer attention map comparisons on the two image inputs (left column of Fig. 3). We crop image patches (in green and orange boxes) at the same locations in (a) and (c) to calculate the self-attention map for other locations.

manifests that the proposed model based on Transformer attention can differentiate the pixel sharpness variance on the image input. Although some attention is put wrongly like in Subfig. (c), where the attention on the monitor and toy is incorrect, the most of attention is distributed consistently

with the input patch appearance. Additionally, the attention of the chosen channel of the Transformer encoder for visualization is not scattered around the whole image, which further discloses that the attention is mainly focused on the similar semantic, sharpness, and appearance information of the input patch.

10. Fusion by LSTM

The LSTM module facilitates our network to fuse each image from the focal stack incrementally, which extends the model capability to varying focal stack lengths. Figure 10 depicts the fusion process of ordered input images of one stack. As the images from the stack are given sequentially, starting from the in-focus plane close to the camera, the model can fuse the sharp in-focus features from various frames to attain a final all-in-focus disparity map at the bottom right.

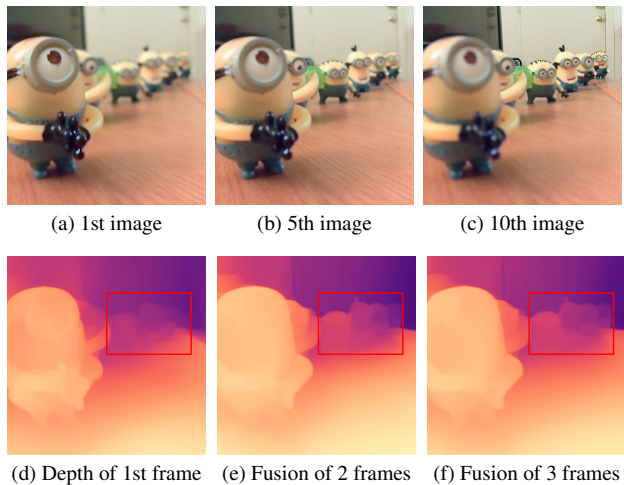


Figure 10. The top row is the input, and the bottom is the output disparity map. The final disparity map is at the bottom right. The red rectangle highlights the incremental fusion results of depth information in the background.

In table 9, we compare our model to its base model without the LSTM module. For the performance without LSTM, the encoder, and decoder are connected directly, and all the depth maps of each image in the stack are averaged to get the metric results of a whole stack. The results indicate the necessity and importance of the LSTM module in depth estimation from the focal stack problem. It further validates that the modeling stack information separately from the image spatial features can help to improve depth prediction accuracy.

11. Network Complexity and Structure Details

Our network comprises the early-stage multi-scale CNN, the Transformer, the LSTM module, and the decoder. We

Structure design	RMSE↓	absRel↓	Bump↓
Model w/o LSTM module	3.68e-2	0.324	0.37
Full model	1.92e-2	0.161	0.19

Table 9. Metric evaluation on different settings for LSTM module on DDFD 12-Scene validation dataset.

present a summary of each module parameter size, real-time Floating-point operations per second (FLOPS), and the inference time,

Module	Params size	Inference Time
Early multi-scale kernel CNNs	0.487M	0.001s
Transformer	42.065M	0.006s
LSTM	15.247M	0.003s
CNN Decoder	16.856M	0.005s
Total	74.655M	0.015

Table 10. Summary of module size, and inference time for processing one image, for the whole stack, the total time is calculated from a whole stack of images’ processing.

From Table 10, we can see the main time consumption is allocated on the Transformer module and decoder, which shows the potential to reduce the model size further can be achieved, *e.g.*, by using MobileViT as an encoder. Our proposed LSTM over the latent feature representation, has a size of only around one-third of Transformer encoder, furthermore, the shallow early multi-scale kernel CNNs is in quite a small size with only 0.487 million parameters and fast processing time around 1ms. The time model size and time complexity summary table further justify our model’s compact and efficient design, where the recurrent LSTM module has benefits both in memory size and computational complexity in the design. The main inference time for a single image processing is from the Transformer Encoder, which can be attributed mainly to the attention computation of multiple self-attention heads, and CNN decoder.

We report the param num in the table below. Although our method contains more parameters (more than half for the Transformer encoder), it increases the performance generally. Our performance gain over the previous competitor is also obvious (with efficient computation as shown in the paper), demonstrating the benefits of using more parameters, *i.e.*, ours gets 0.024 gain on logRMSE using about 2 times param of DFVNet, while DFVNet gets 0.02 gain vs DefocusNet by using about 3 times param of DefocusNet.

	DDFFNet	DefocusNet	DFVNet	Ours
Param Num	≈40M	≈18M	≈56M	≈75M
logRMSE	0.320	0.230	0.210	0.186

We present the three main components of our model in Fig. 11, 12, and 13, respectively.

The early-stage multi-scale CNN in Fig. 11 takes images from the focal stacks incrementally, *i.e.* a single image $(1, 3, H, W)$ at a time. The H , and W denote the image’s height and width, respectively. In each figure, the output tensor shape is presented inside the parentheses next to each

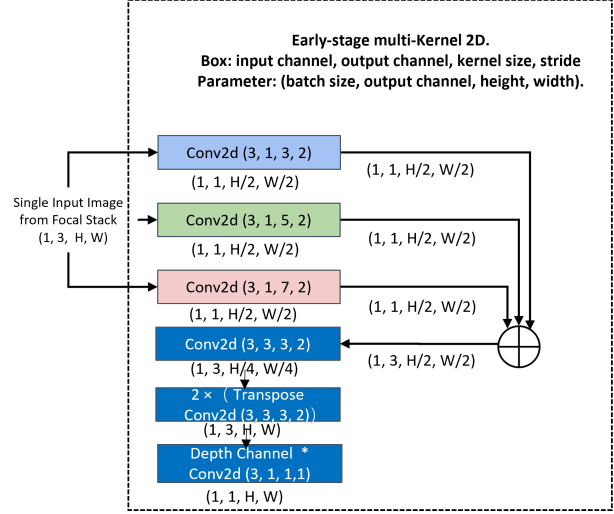


Figure 11. The structure details of early-stage multi-scale kernel CNN along with the output size of each layer. The convolution and transpose convolution after concatenation generate a feature map followed by a 1×1 convolution along depth channel.

box. We present each 2D convolution layer with the input feature dimension, output feature dimension, the kernel size and stride inside the parentheses. The early-stage multi-scale CNN generates a feature map of size $(1, 1, H, W)$. The bottom blue boxes in the figure are referred to as “depth channel convolution” in our paper.

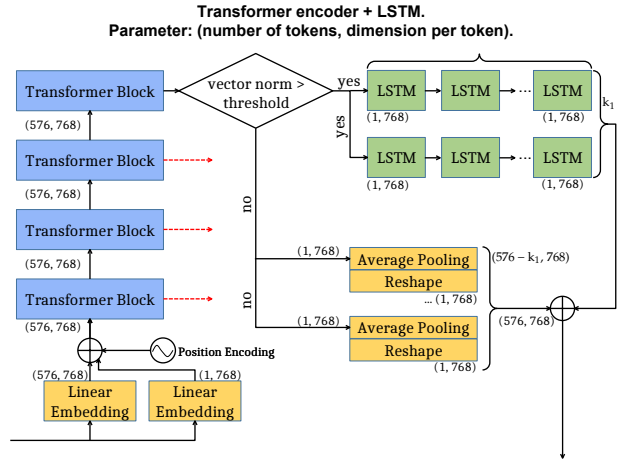


Figure 12. The LSTM-Transformer block with token size and token dimension.

The linear embedding layer (Fig. 12) takes the feature map from early-stage multi-scale kernel convolution, to project into corresponding local patch tokens and a single global token for the whole feature map. The local tokens, the global token, and the position encoding are fused together before being given to the transformer encoder. The

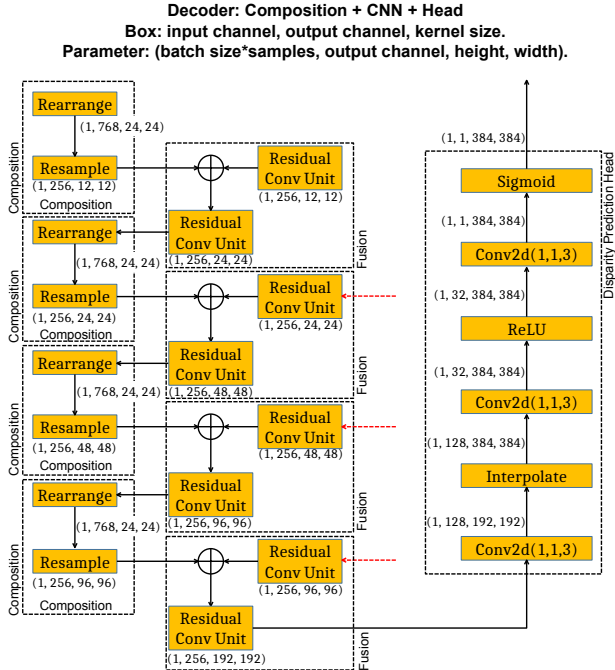


Figure 13. The decoder is composed of repeating composition and fusion modules. The output size of each layer is presented in parenthesis next to the box.

output tokens of the last transformer block are grouped based on the vector norm of each token, big norms above a threshold are considered activation tokens, while the rest are regarded as non-activation tokens. The k_1 activation tokens are given to the LSTM blocks (Fig. 12), while we apply average pooling on other $576 - k_1$ non-activation tokens. Finally, we add these two groups of tokens to shape the same tokens’ arrangement as the input, and then these filtered tokens are delivered to the decoder in Fig. 13. We present the whole network structure in Fig. 18.

12. Quantitative results on LightField4D

We present the quantitative results for cross-dataset evaluation of our model on the LightField4D dataset in Table 11. Our model achieves a comparable performance in terms of accuracy (58.90%) on this completely unseen dataset. Although the AiFNet can attain the least RMSE (0.231) and logRMSE(0.407) error, our model generates smoother boundaries and fine-grained details, indicated by a lower bumpiness value (2.53). We use the available pre-trained AiFNet on LightField3D which uses the all-in-focus color image as supervision for evaluation. It also explains why AiFNet achieves satisfactory performance, and it further validates our model’s good generability without using any supervision signal from this new focal stack dataset, while

our model can achieve plausible performance only by learning a good stack distribution and spatial sharp feature representation from DDFD 12-Scene dataset.

Model	RMSE↓	logRMSE↓	absRel↓	Bump↓	$\delta(1.25)$ ↑
DDFFNet	0.431	0.790	0.761	2.93	44.39
DefocusNet	0.273	0.471	0.435	2.84	48.73
DFVNet	0.352	0.647	0.594	2.97	43.54
AiFNet	0.231	0.407	0.374	2.53	55.04
Ours	0.237	0.416	0.364	1.54	58.90

Table 11. Metric evaluation results on ”additional” set of LightField4D dataset. The best results are denoted in **Red**, while **Blue** indicates the second-best.

13. Visual results

In this section, we present the additional visual comparison results of our model on DDFD 12-Scene, Mobile Depth, and LightField 4D datasets in Fig. 14, 15, 16, 17, respectively. All comparison results include ground truths except the Mobile Depth dataset, captured by cellphones.

Visual Results on DDFD 12-Scene Dataset. Fig. 14 shows examples of depth prediction of our model on an additional set of samples from the DDFD 12-Scene validation set. We show that our model preserves a lot of local details on disparity map, e.g., books on the shelf (first row), the chair (second row), and the black-colored couch in the top-left corner (last row). Our model predicts an accurate depth with sharper and smoother boundaries compared to prior works.

Visual Results on FOD500 Dataset. We report our qualitative results on the last 100 images of the FOD-500 dataset in Fig. 15 to compare them with prior works. We observe decent disparity prediction results with smoother boundaries and preserved local structure details, e.g., the center hole (last row) and the small hole at the top center (sixth row). The DDFDNet and DefocusNet are fine-tuned on FOD-500 with their weights pre-trained on DDFD 12-Scene dataset. We achieve comparable performance to DFVNet and AiFNet, yet better than other prior works.

Visual Results on Mobile Depth Dataset. Fig. 16 depicts the additional visual results of our model on Mobile Depth dataset for cross-dataset evaluation on *varying focal stack length*. The figure shows that our model consistently predicts accurate disparity from an arbitrary number of images in focal stacks, although it has never been trained on this dataset. In comparison to prior works, our model achieves better estimations that predict sharp and crisp boundaries, e.g., the metal tap (second row), the plant (third row) and the ball next to the window (last row). Also the mirror effects pose a big challenge to our model, as visualized in the last row at the window background.

Visual Results on LightField4D Dataset. We present an additional set of visual results of our model on LightField4D dataset in Fig. 17. More specifically, we employ

the "additional set" from the dataset for cross-dataset evaluation. Our model estimates better depth on this unseen dataset, that preserves the local details in many complex structures, *e.g.*, the tower (first row), board game (second row), and the tomb (fifth row). Our model achieves a deficit performance in shadow, and textureless scenes, such as the pillow (last row) and "Antinous" (sixth row).

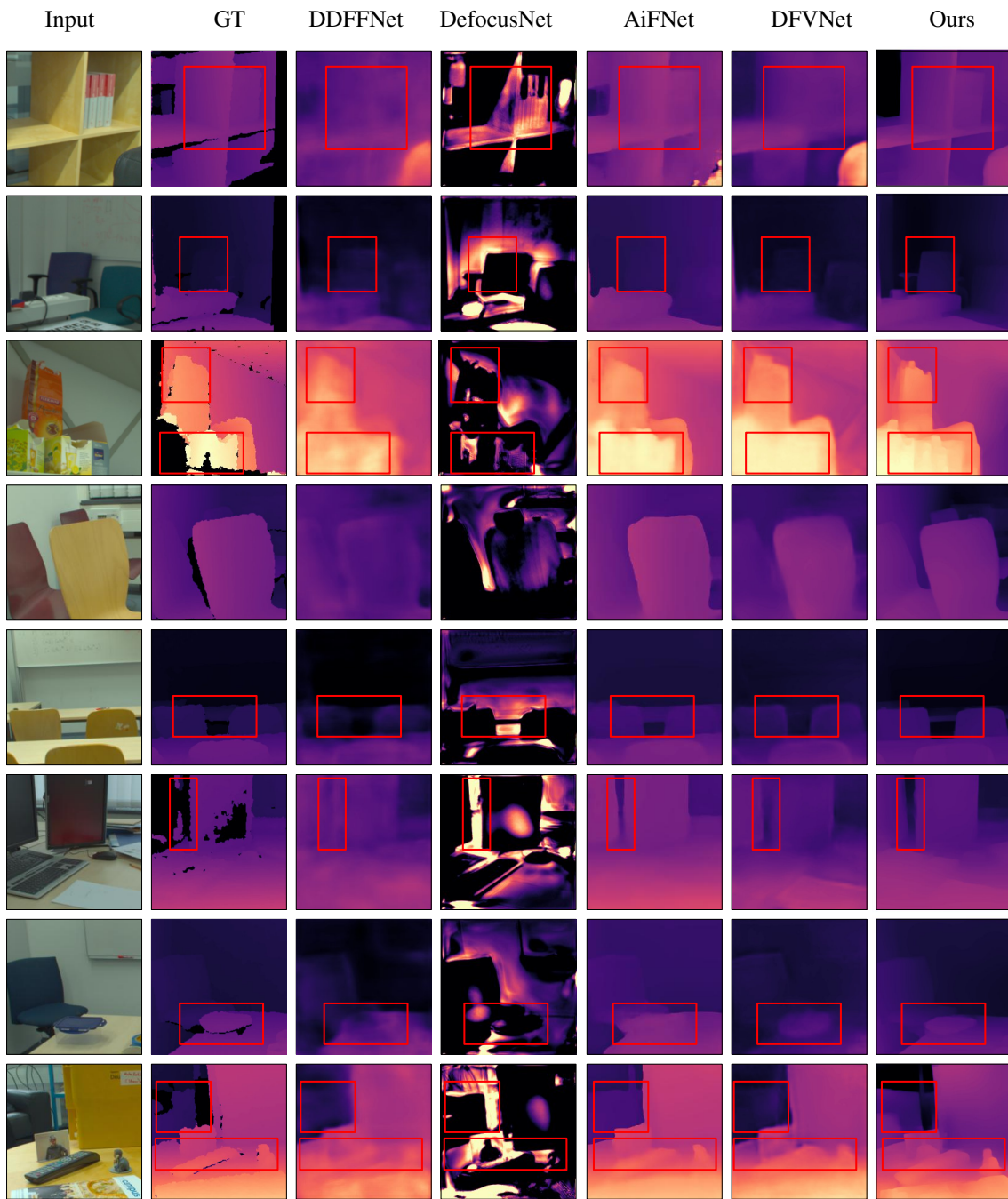


Figure 14. Qualitative evaluation of our model on DDFF 12-Scene dataset validation set.



Figure 15. Qualitative evaluation of our model on FOD500 dataset. Only the last 100 focal stacks are used for testing. DFVNet uses first 400 focal stacks for training and other models use the same split for fine-tuning.

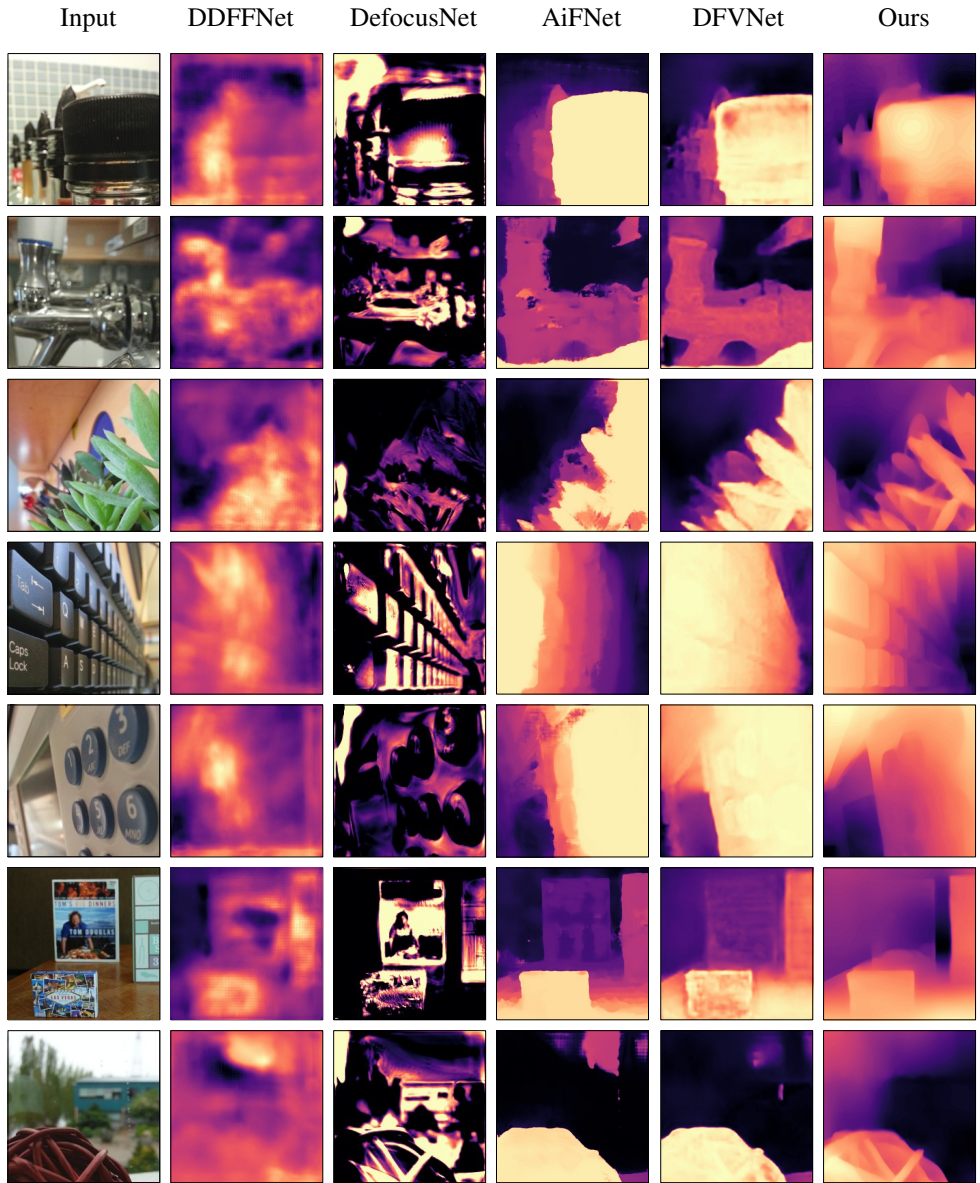


Figure 16. Qualitative evaluation of our model on Mobile Depth dataset. This dataset contains focal stacks of varying lengths and image sizes, we cropped raw image inputs from the top left.

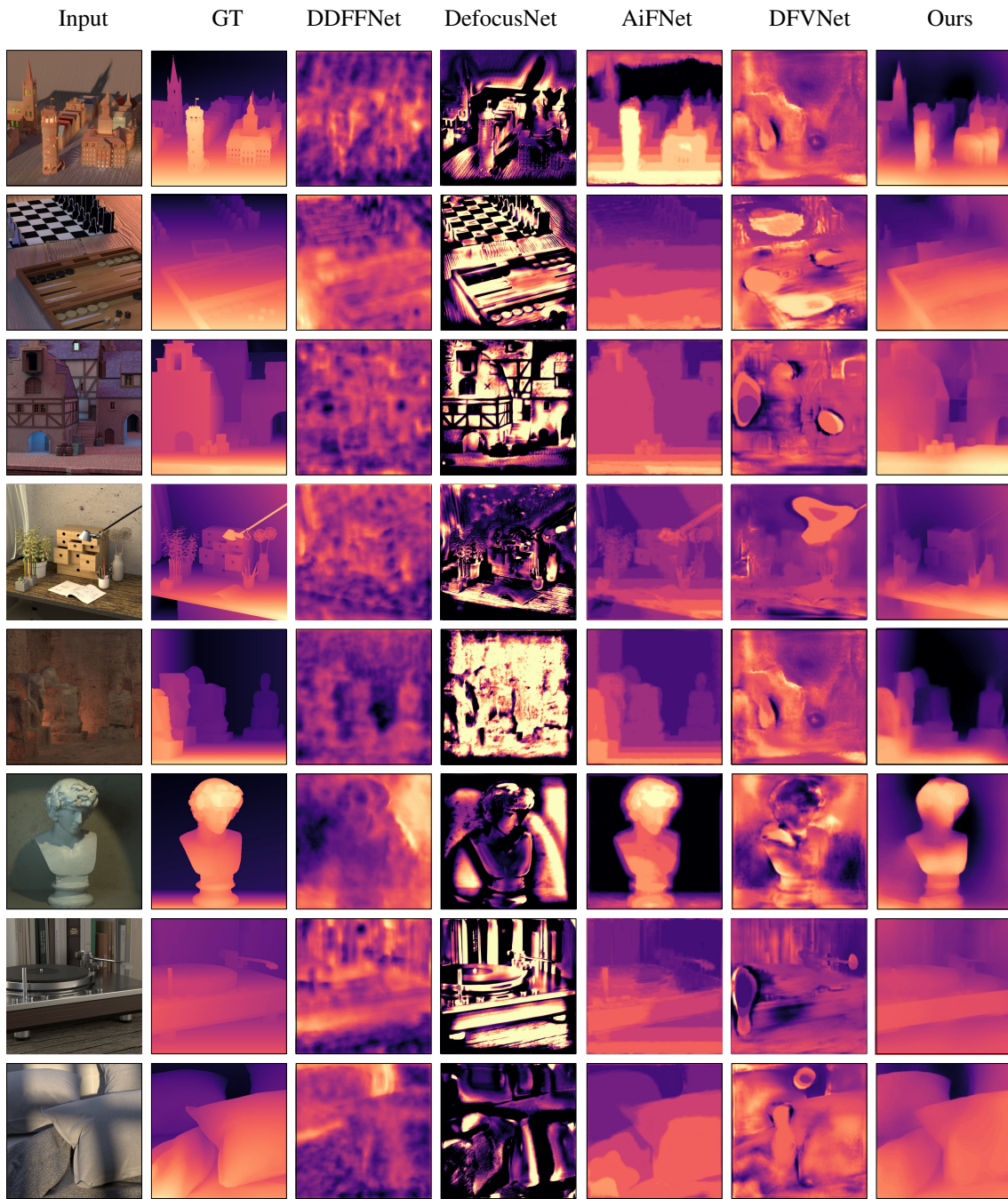


Figure 17. Qualitative evaluation of our model on an additional set of LightField4D dataset.

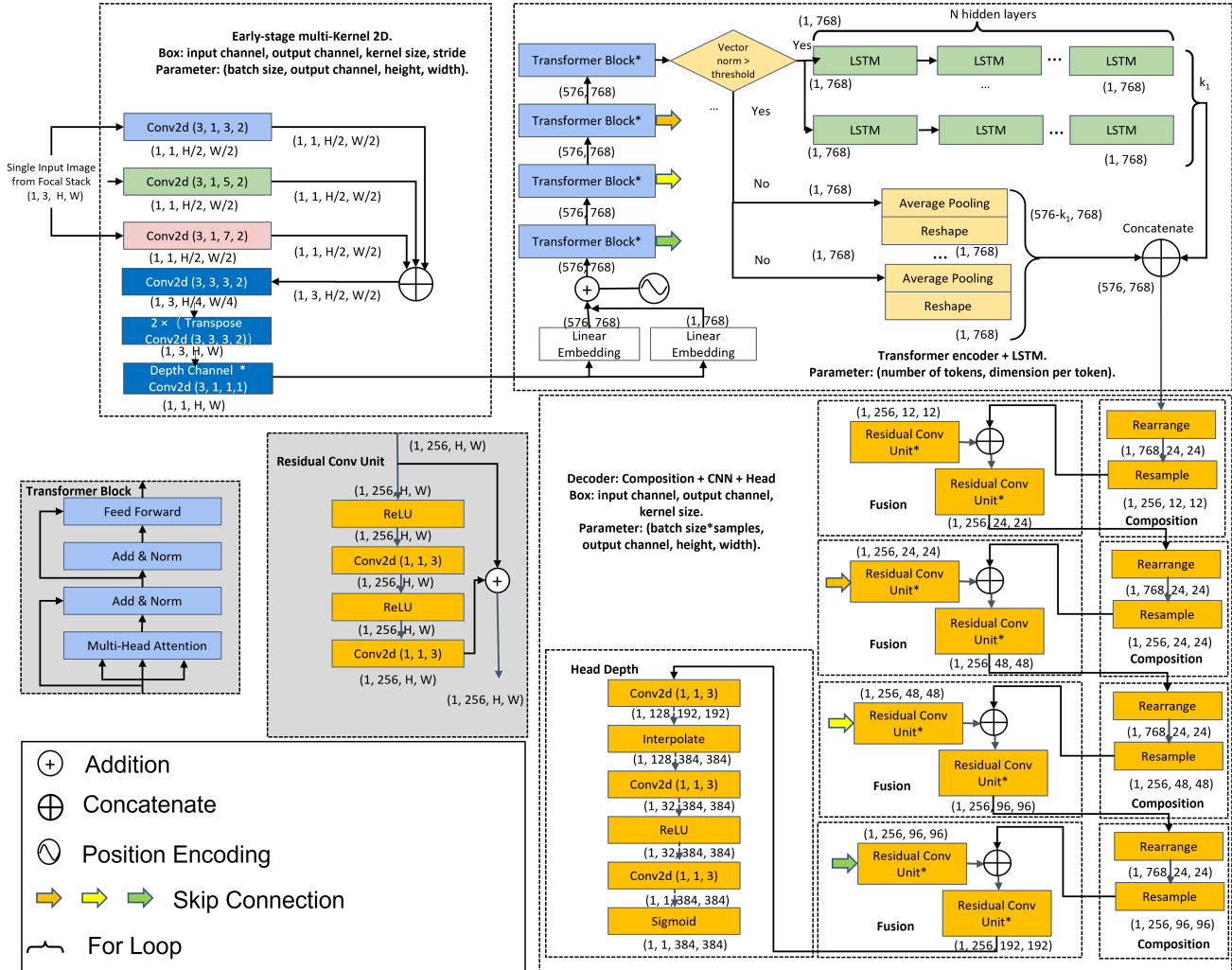


Figure 18. The overview structure of our model with notations about the output size of each layer, and the convolution parameters in the parenthesis. The top left is early-stage multi-scale kernel convolution, the top right is the LSTM-Transformer block, and the bottom right is the decoder, including the repeating compositions and fusions, and a final disparity head.

FocDepthFormer: Transformer with LSTM for Depth Estimation from Focus – Supplementary Materials

1. Focal principles

In the paper we present the features of our network model, a primary factor to explain our favorable results is the good identification ability of pixel sharpness, as mentioned in our paper. Usually, the sharpness of pixels can be evaluated according to the Circle-of-Confusion, C (in Fig. 1), defined as follows,

$$C = \frac{f^2}{N(z - d_f)} \left| 1 - \frac{d_f}{z} \right|, \quad (1)$$

where, N denotes f -number, as a ratio of focal length to the valid aperture diameter. C is the Circle of Confusion (CoC) diameter. d_f is the focus distance of the lens. z represents the distance from the lens to the target object. In general, the range of z is $[0, \infty]$. However, in reality, the range is always constrained by lower and upper bounds.

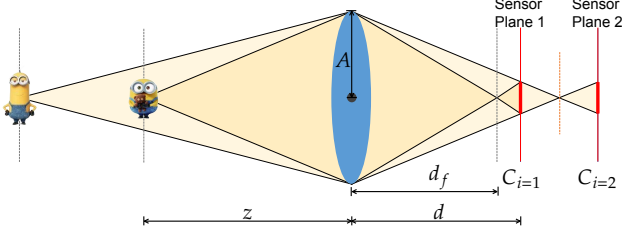


Figure 1. The rays emitted from an object placed at an axial distance z to the lens, converging at a distance d_f behind the lens. Sensor is situated at a distance d from focal lens. The pixels are sharply imaged when the sensor is placed right at focus distance, C is the CoC, that grows as the sensor position is deviated from the focus plane.

In Eq. 1, C is zero (C^*) when the image pixel is in-focus, and it is a signed value, where $C > 0$ indicates the camera focused in front of the sensor plane, while $C < 0$ is the reverse case, with camera focused behind the sensor plane. It can be inferred from the denominator, CoC C has two divergence points, at 0 and d_f respectively. Our model actually learn the mapping relationship from CoC to depth autonomously.

2. Metrics

The metrics used in our work for quantitative evaluations, are defined as follows,

$$RMSE : \sqrt{\frac{1}{|M|} \sum_{p \in \mathbf{x}} \|f(\mathbf{x}) - \mathbf{D}\|^2}, \quad (2)$$

$$\log RMSE : \sqrt{\frac{1}{|M|} \sum_{p \in \mathbf{x}} \|\log f(\mathbf{x}) - \mathbf{D}\|^2}, \quad (3)$$

$$absRel : \frac{1}{|M|} \sum_{p \in \mathbf{x}} \frac{|f(\mathbf{x}) - \mathbf{D}|}{\mathbf{D}}, \quad (4)$$

$$sqrRel : \frac{1}{|M|} \sum_{p \in M} \frac{\|f(\mathbf{x}) - \mathbf{D}\|}{\mathbf{D}}, \quad (5)$$

$$Bump : \frac{1}{|M|} \sum_{p \in \mathbf{x}} \min(0.05, \|\mathbf{H}_\Delta(p)\|) \times 100, \quad (6)$$

$$Accuracy(\delta) : \max\left(\frac{f(\mathbf{x})}{\mathbf{D}}, \frac{\mathbf{D}}{f(\mathbf{x})}\right) = \delta < threshold, \\ \% \text{ of } \mathbf{D}, \quad (7)$$

where $\Delta = f(\mathbf{x}) - \mathbf{D}$ and \mathbf{H} is the Hessian matrix.

3. Effects of focal stack size

We perform extensive experiments to observe the effects of our model on various focal stack sizes. Fig. 2 shows the findings of our experiments on a focal stack from the DDFD 12-Scene validation set, with multiple objects placed at varying depths. In the figure, we plot RMSE and accuracy (in percentage) ($\delta = 1.25$) w.r.t. the number of focal stack images. We observe that the model accuracy increases with more input images from the focal stack in use, while the RMSE decreases correspondingly. Our model achieves a decent performance by six frames from a focal stack, which already captures good spatial and stack dimension information for depth cue estimation usually after 6 frames in use.

4. Attention map

From the comparison figures, it is obvious that the attention of the Transformer module can attend to more in-focus feature information, *i.e.*, the toy on the right side of Subfig. (d) is with higher attention compared to Subfig. (b) at the same location. It shows that the patches can attend to the fore- and background regions with related focus and defocus cues of corresponding depth field quite well. It further manifests that the proposed model based on Transformer attention can differentiate the pixel sharpness variance on the

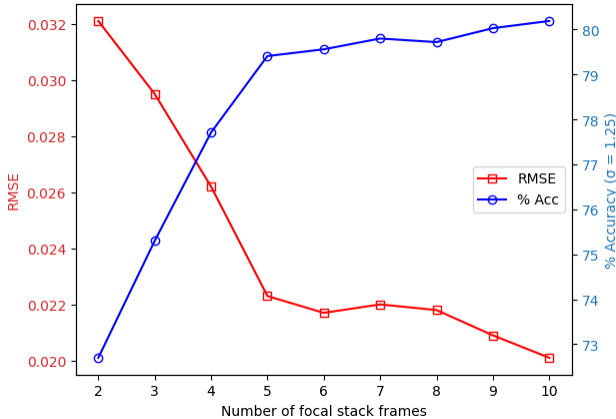


Figure 2. Our model performance w.r.t. the frame size of one focal stack sample from DDFD 12-Scene test.



Figure 3. These subfigures are used as complementary materials to Fig. 3 of the paper, in order to show the complete Transformer attention map comparisons on the two image inputs (left column of Fig. 3). We crop image patches (in green and orange boxes) at the same locations in (a) and (c) to calculate the self-attention map for other locations.

image input. Although some attention is put wrongly like in Subfig. (c), where the attention on the monitor and toy is incorrect, the most of attention is distributed consistently with the input patch appearance. Additionally, the attention of the chosen channel of the Transformer encoder for vi-

ualization is not scattered around the whole image, which further discloses that the attention is mainly focused on the similar semantic, sharpness, and appearance information of the input patch.

5. Fusion by LSTM

The LSTM module facilitates our network to fuse each image from the focal stack incrementally, which extends the model capability to varying focal stack lengths. Figure 4 depicts the fusion process of ordered input images of one stack. As the images from the stack are given sequentially, starting from the in-focus plane close to the camera, the model can fuse the sharp in-focus features from various frames to attain a final all-in-focus disparity map at the bottom right.

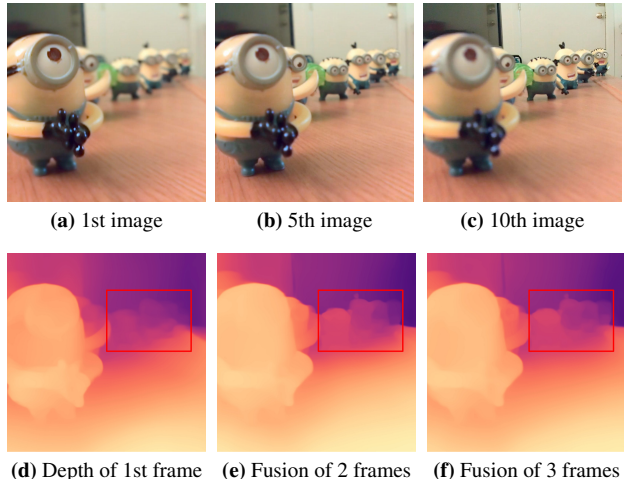


Figure 4. The top row is the input, and the bottom is the output disparity map. The final disparity map is at the bottom right. The red rectangle highlights the incremental fusion results of depth information in the background.

In table 1, we compare our model to its base model without the LSTM module. For the performance without LSTM, the encoder, and decoder are connected directly, and all the depth maps of each image in the stack are averaged to get the metric results of a whole stack. The results indicate the necessity and importance of the LSTM module in depth estimation from the focal stack problem. It further validates that the modeling stack information separately from the image spatial features can help to improve depth prediction accuracy.

Structure design	RMSE↓	absRel↓	Bump↓
Model w/o LSTM module	3.68e-2	0.324	0.37
Full model	1.92e-2	0.161	0.19

Table 1. Metric evaluation on different settings for LSTM module on DDFD 12-Scene validation dataset.

6. Network Complexity and Structure Details

Our network comprises the early-stage multi-scale CNN, the Transformer, the LSTM module, and the decoder. We present a summary of each module parameter size, real-time Floating-point operations per second (FLOPS), and the inference time,

Module	Params size	Inference Time
Early multi-scale kernel CNNs	0.487M	0.001s
Transformer	42.065M	0.006s
LSTM	15.247M	0.003s
CNN Decoder	16.856M	0.005s
Total	74.655M	0.015

Table 2. Summary of module size, and inference time for processing one image, for the whole stack, the total time is calculated from a whole stack of images’ processing.

From Table 2, we can see the main time consumption is allocated on the Transformer module and decoder, which shows the potential to reduce the model size further can be achieved, *e.g.*, by using MobileViT as an encoder. Our proposed LSTM over the latent feature representation, has a size of only around one-third of Transformer encoder, furthermore, the shallow early multi-scale kernel CNNs is in quite a small size with only 0.487 million parameters and fast processing time around 1ms. The time model size and time complexity summary table further justify our model’s compact and efficient design, where the recurrent LSTM module has benefits both in memory size and computational complexity in the design. The main inference time for a single image processing is from the Transformer Encoder, which can be attributed mainly to the attention computation of multiple self-attention heads, and CNN decoder.

We report the param num in the table below. Although our method contains more parameters (more than half for the Transformer encoder), it increases the performance generally. Our performance gain over the previous competitor is also obvious (with efficient computation as shown in the paper), demonstrating the benefits of using more parameters, *i.e.*, ours gets 0.024 gain on logRMSE using about 2 times param of DFVNet, while DFVNet gets 0.02 gain vs DefocusNet by using about 3 times param of DefocusNet.

	DDFFNet	DefocusNet	DFVNet	Ours
Param Num	≈40M	≈18M	≈56M	≈75M
logRMSE	0.320	0.230	0.210	0.186

We present the three main components of our model in Fig. 5, 6, and 7, respectively.

The early-stage multi-scale CNN in Fig. 5 takes images from the focal stacks incrementally, *i.e.* a single image $(1, 3, H, W)$ at a time. The H , and W denote the image’s height and width, respectively. In each figure, the output tensor shape is presented inside the parentheses next to each

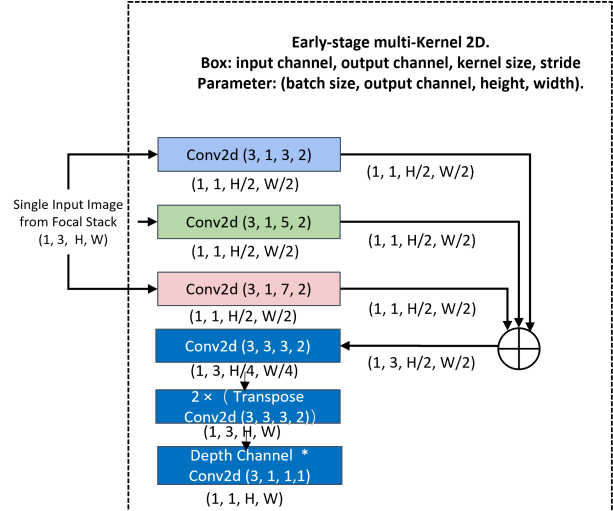


Figure 5. The structure details of early-stage multi-scale kernel CNN along with the output size of each layer. The convolution and transpose convolution after concatenation generate a feature map followed by a 1×1 convolution along depth channel.

box. We present each 2D convolution layer with the input feature dimension, output feature dimension, the kernel size and stride inside the parentheses. The early-stage multi-scale CNN generates a feature map of size $(1, 1, H, W)$. The bottom blue boxes in the figure are referred to as “depth channel convolution” in our paper.

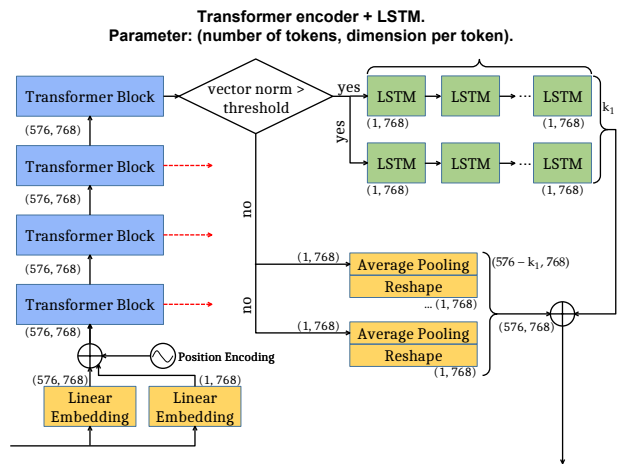


Figure 6. The LSTM-Transformer block with token size and token dimension.

The linear embedding layer (Fig. 6) takes the feature map from early-stage multi-scale kernel convolution, to project into corresponding local patch tokens and a single global token for the whole feature map. The local tokens,

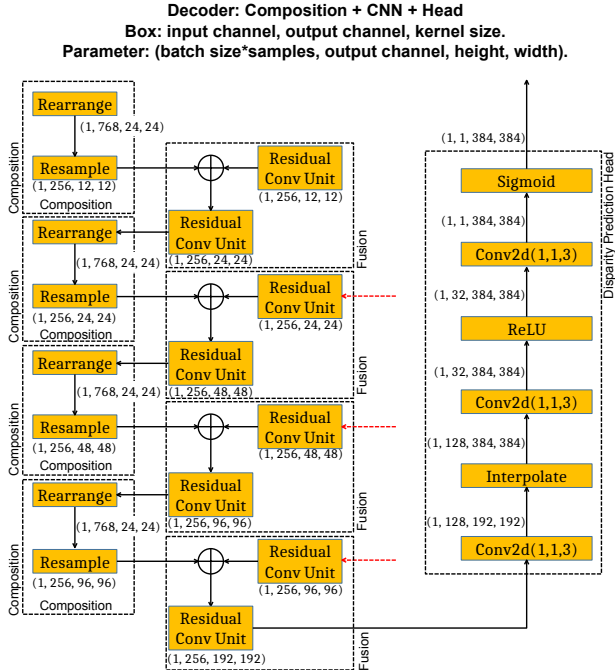


Figure 7. The decoder is composed of repeating composition and fusion modules. The output size of each layer is presented in parenthesis next to the box.

the global token, and the position encoding are fused together before being given to the transformer encoder. The output tokens of the last transformer block are grouped based on the vector norm of each token, big norms above a threshold are considered activation tokens, while the rest are regarded as non-activation tokens. The k_1 activation tokens are given to the LSTM blocks (Fig. 6), while we apply average pooling on other $576 - k_1$ non-activation tokens. Finally, we add these two groups of tokens to shape the same tokens’ arrangement as the input, and then these filtered tokens are delivered to the decoder in Fig. 7. We present the whole network structure in Fig. 12.

7. Quantitative results on LightField4D

We present the quantitative results for cross-dataset evaluation of our model on the LightField4D dataset in Table 3. Our model achieves a comparable performance in terms of accuracy (58.90%) on this completely unseen dataset. Although the AiFNet can attain the least RMSE (0.231) and logRMSE(0.407) error, our model generates smoother boundaries and fine-grained details, indicated by a lower bumpiness value (2.53). We use the available pre-trained AiFNet on LightField3D which uses the all-in-focus color image as supervision for evaluation. It also explains why AiFNet achieves satisfactory performance, and it further

validates our model’s good generability without using any supervision signal from this new focal stack dataset, while our model can achieve plausible performance only by learning a good stack distribution and spatial sharp feature representation from DDFF 12-Scene dataset.

Model	RMSE↓	logRMSE↓	absRel↓	Bump↓	$\delta(1.25) \uparrow$
DDFFNet	0.431	0.790	0.761	2.93	44.39
DefocusNet	0.273	0.471	0.435	2.84	48.73
DFVNet	0.352	0.647	0.594	2.97	43.54
AiFNet	0.231	0.407	0.374	2.53	55.04
Ours	0.237	0.416	0.364	1.54	58.90

Table 3. Metric evaluation results on “additional” set of LightField4D dataset. The best results are denoted in **Red**, while **Blue** indicates the second-best.

8. Visual results

In this section, we present the additional visual comparison results of our model on DDFF 12-Scene, Mobile Depth, and LightField 4D datasets in Fig. 8, 9, 10, 11, respectively. All comparison results include ground truths except the Mobile Depth dataset, captured by cellphones.

Visual Results on DDFF 12-Scene Dataset. Fig. 8 shows examples of depth prediction of our model on an additional set of samples from the DDFF 12-Scene validation set. We show that our model preserves a lot of local details on disparity map, *e.g.*, books on the shelf (first row), the chair (second row), and the black-colored couch in the top-left corner (last row). Our model predicts an accurate depth with sharper and smoother boundaries compared to prior works.

Visual Results on FOD500 Dataset. We report our qualitative results on the last 100 images of the FOD-500 dataset in Fig. 9 to compare them with prior works. We observe decent disparity prediction results with smoother boundaries and preserved local structure details, *e.g.*, the center hole (last row) and the small hole at the top center (sixth row). The DDFFNet and DefocusNet are fine-tuned on FOD-500 with their weights pre-trained on DDFF 12-Scene dataset. We achieve comparable performance to DFVNet and AiFNet, yet better than other prior works.

Visual Results on Mobile Depth Dataset. Fig. 10 depicts the additional visual results of our model on Mobile Depth dataset for cross-dataset evaluation on *varying focal stack length*. The figure shows that our model consistently predicts accurate disparity from an arbitrary number of images in focal stacks, although it has never been trained on this dataset. In comparison to prior works, our model achieves better estimations that predict sharp and crisp boundaries, *e.g.*, the metal tap (second row), the plant (third row) and the ball next to the window (last row). Also the mirror effects pose a big challenge to our model, as visualized in the last row at the window background.

Visual Results on LightField4D Dataset. We present an additional set of visual results of our model on LightField4D dataset in Fig. 11. More specifically, we employ the “additional set” from the dataset for cross-dataset evaluation. Our model estimates better depth on this unseen dataset, that preserves the local details in many complex structures, *e.g.*, the tower (first row), board game (second row), and the tomb (fifth row). Our model achieves a deficit performance in shadow, and textureless scenes, such as the pillow (last row) and “Antinous” (sixth row).

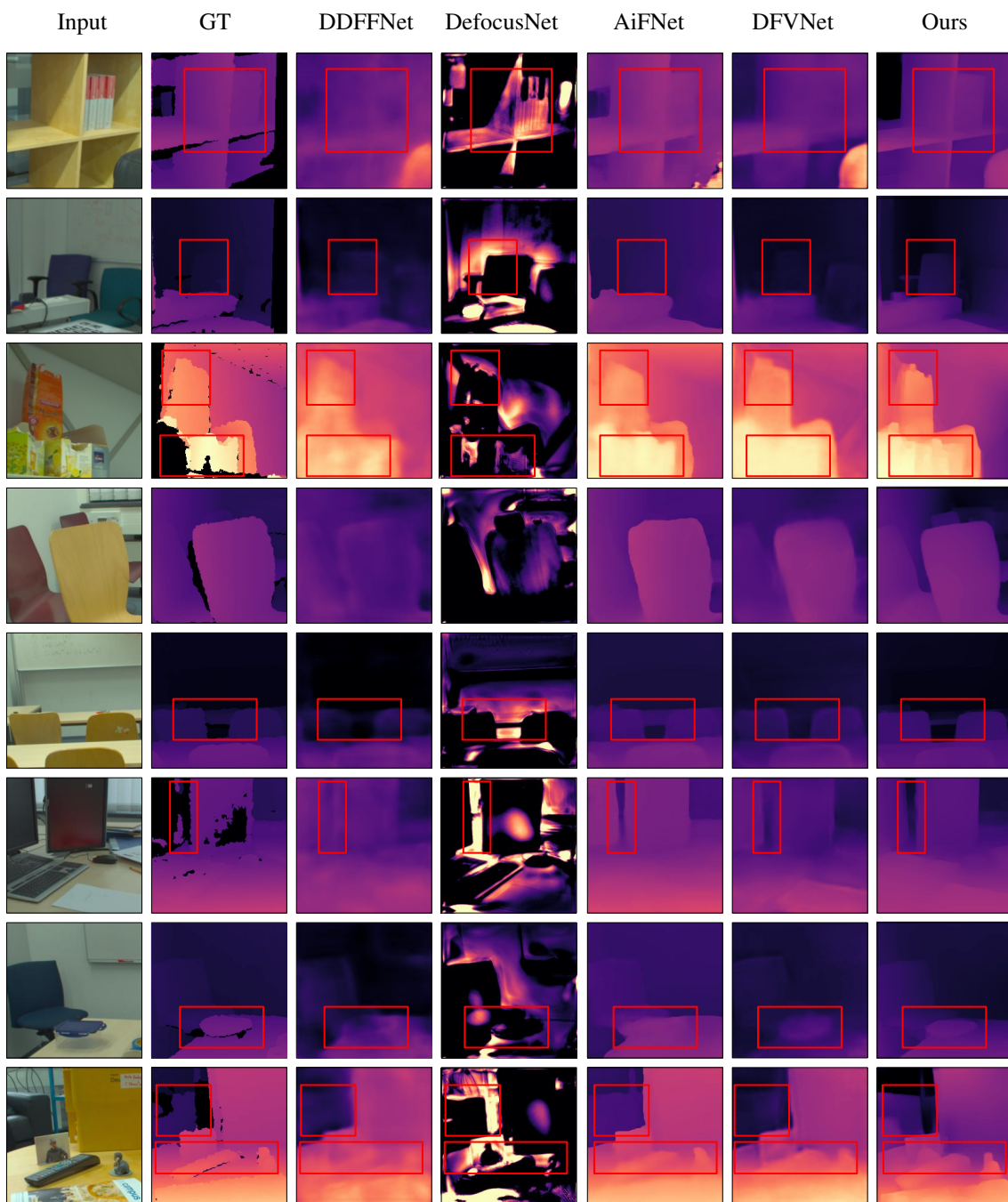


Figure 8. Qualitative evaluation of our model on DDFF 12-Scene dataset validation set.

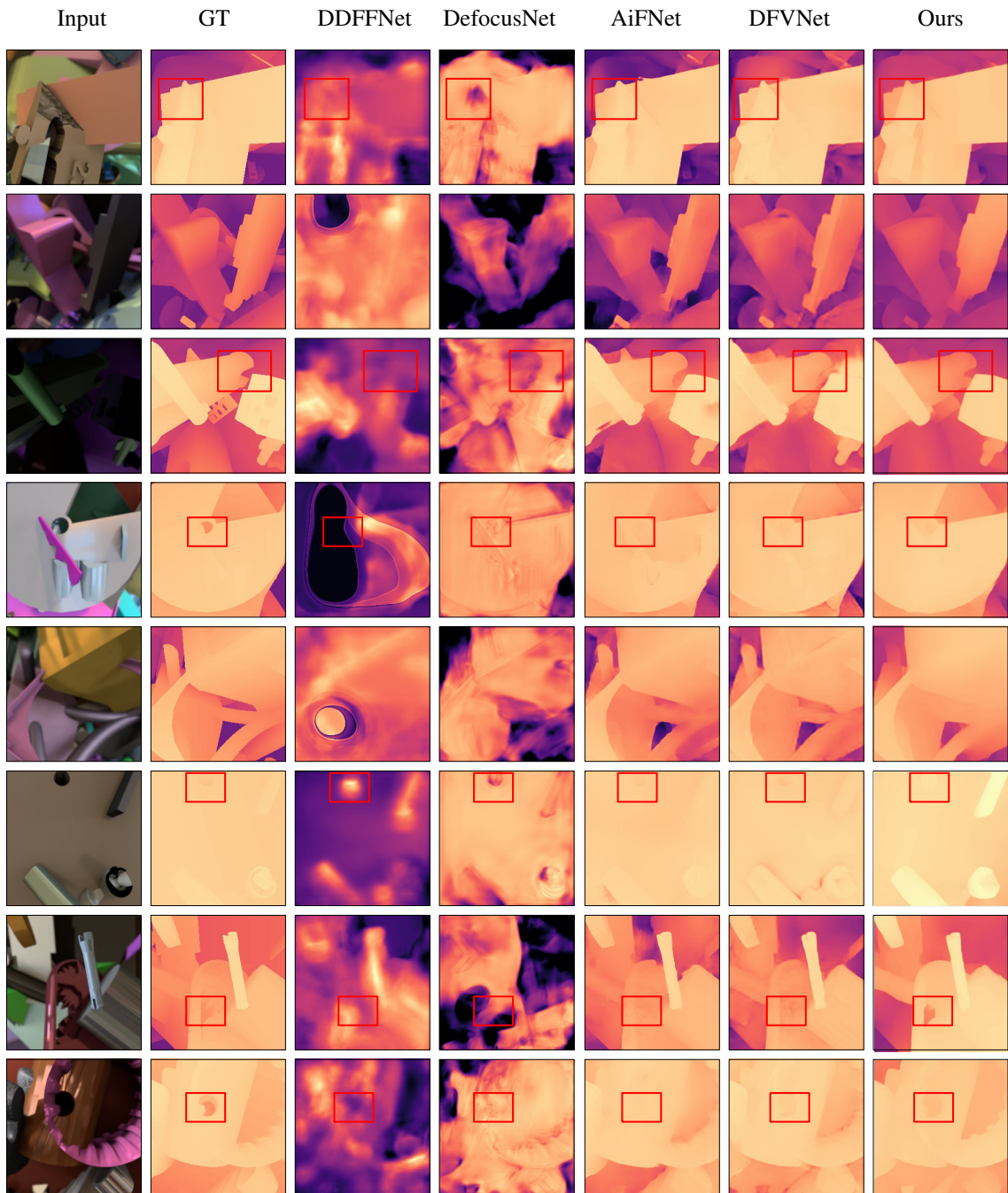


Figure 9. Qualitative evaluation of our model on FOD500 dataset. Only the last 100 focal stacks are used for testing. DFVNet uses first 400 focal stacks for training and other models use the same split for fine-tuning.

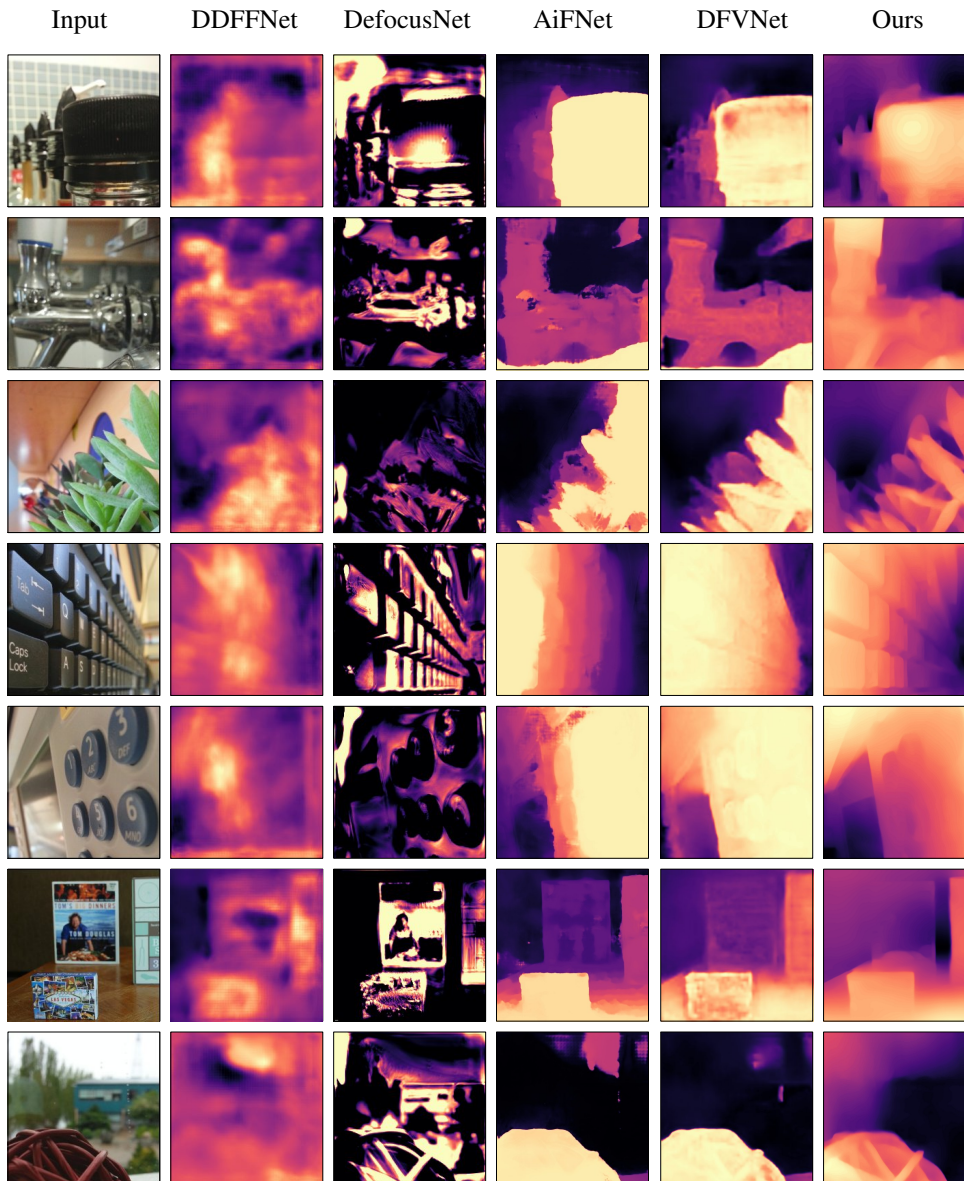


Figure 10. Qualitative evaluation of our model on Mobile Depth dataset. This dataset contains focal stacks of varying lengths and image sizes, we cropped raw image inputs from the top left.

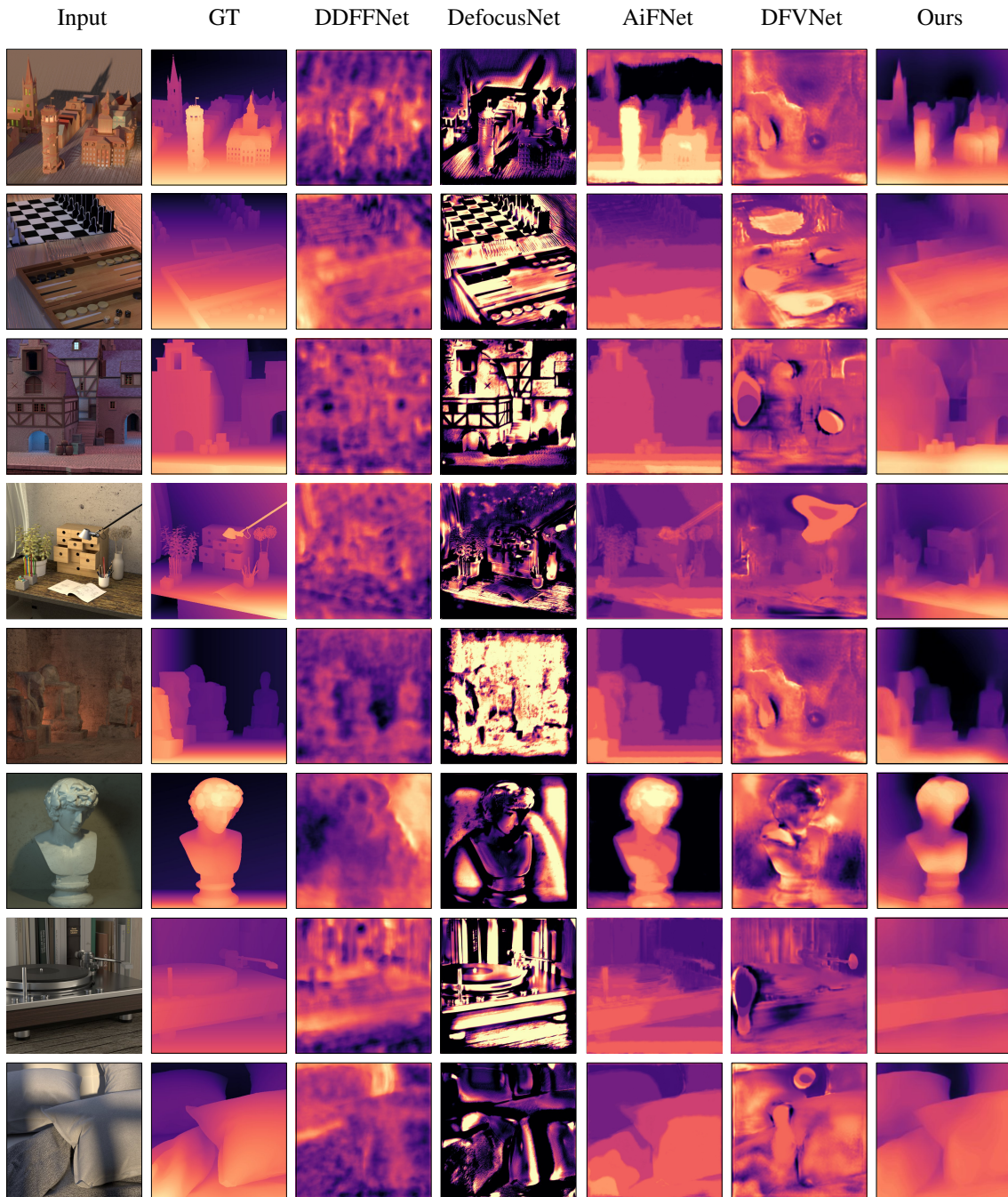


Figure 11. Qualitative evaluation of our model on an additional set of LightField4D dataset.

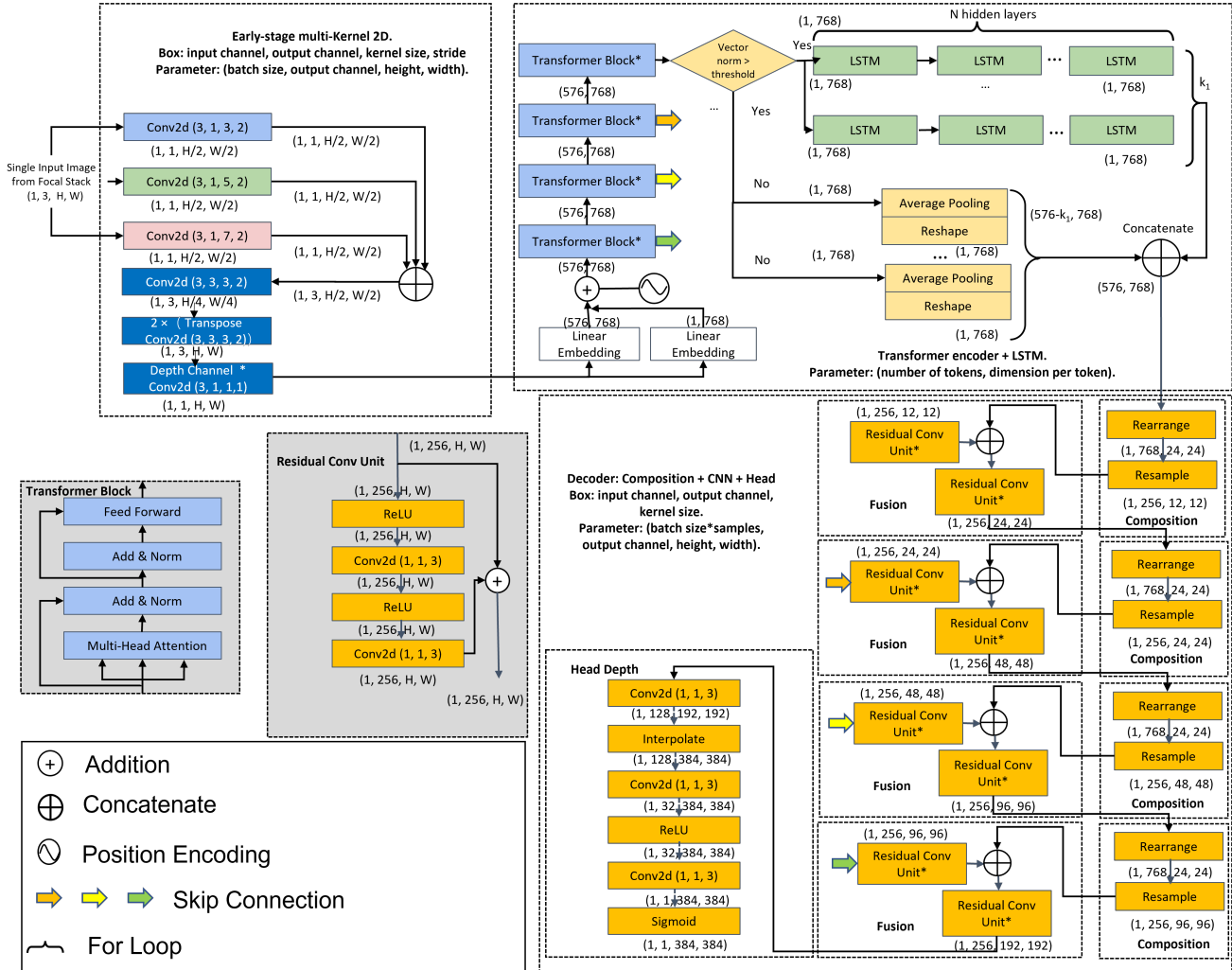


Figure 12. The overview structure of our model with notations about the output size of each layer, and the convolution parameters in the parenthesis. The top left is early-stage multi-scale kernel convolution, the top right is the LSTM-Transformer block, and the bottom right is the decoder, including the repeating compositions and fusions, and a final disparity head.